Supplementary Information (SI) for Chemical Science.

Supporting Information: The fine effects of high magnetic fields on hyperfine shifts

Letizia Fiorucci[1,2,3], Lucas Lang[4], David L. Tierney[5], Mauro Botta[6], Giacomo Parigi[1,2,7], Claudio Luchinat[1,2,7], and Enrico Ravera[1,2,7,8]

[1]Department of Chemistry "Ugo Schiff" and Magnetic Resonance Center (CERM), University of Florence, 50019 Florence, Italy
[2]Consorzio Interuniversitario Risonanze Magnetiche di Metalloproteine (CIRMMP), 50019 Florence, Italy
[3]Present address: Max-Planck-Institut für Kohlenforschung, Kaiser-Wilhelm-Platz 1, 45470 Mülheim an der Ruhr, Germany
[4]Technische Universität Berlin, Institut für Chemie, Theoretische Chemie/Quantenchemie, Sekr. C7, Straße des 17. Juni 135, 10623 Berlin, Germany
[5]Department of Chemistry and Biochemistry, Miami University, Oxford, OH 45056
[6]Dipartimento di Scienze e Innovazione Tecnologica, Università del Piemonte Orientale, Alessandria, Italy
[7]Giotto Biotech S.R.L, Sesto Fiorentino, 50019, Italy
[8]Florence Data Science, University of Florence, 50134 Florence, Italy

Contents

S1 Connection of terms in equation 1 to the self-orientation tensor

In the formulation introduced by Equation 1 of the main text, the hyperfine shifts affected by the indirect field contribution are defined as

$$\delta \approx -\frac{1}{3}\boldsymbol{\sigma}^{(2:1)} + \left[\frac{1}{45}\frac{\beta}{\mu_0}\boldsymbol{\sigma}^{(2:1)}\boldsymbol{\chi}^{(2:1)} - \frac{1}{15}\frac{\beta}{\mu_0}(\boldsymbol{\sigma}\boldsymbol{\chi})^{(2:1)}\right] B_0^2 \tag{S1}$$

It can be shown that this equation is exactly identical to the one commonly presented in the literature to account for field-induced self-orientation in solution[1]:

$$\delta \approx -\boldsymbol{\sigma}\boldsymbol{P} \tag{S2}$$

where the elements of $\boldsymbol{P}$ are defined in Equation 4 of the main text, which can also be rewritten as:

$$P_{ll} = \frac{1}{3}\left[1 + \frac{B_0^2}{5}\frac{\beta}{\mu_0}\left(\chi_{ll} - \chi_{\text{iso}}\right)\right], \tag{S3}$$

with $\chi_{\text{iso}} = \boldsymbol{\chi}^{(2:1)}/3$. By equating Equation S1 and S2 in the reference frame of $\boldsymbol{\chi}$, one obtains

$$-\frac{1}{3}\sum \sigma_{ii} + \left[\frac{1}{45}\frac{\beta}{\mu_0}\sum \sigma_{ii}\sum \chi_{jj} - \frac{1}{15}\frac{\beta}{\mu_0}\sum \sigma_{ii}\chi_{ii}\right] B_0^2 = -\frac{1}{3}\sum \sigma_{ii}\left[1 + \frac{B_0^2}{5}\frac{\beta}{\mu_0}\left(\chi_{ii} - \frac{\sum \chi_{jj}}{3}\right)\right], \tag{S4}$$

omitting the terms related to the field-independent part, this becomes:

$$\frac{1}{3}\frac{\beta}{\mu_0}\frac{B_0^2}{5}\left[\frac{1}{3}\sum \sigma_{ii}\sum \chi_{jj} - \sum \sigma_{ii}\chi_{ii}\right] = -\frac{1}{3}\frac{\beta}{\mu_0}\frac{B_0^2}{5}\sum \sigma_{ii}\left[\left(\chi_{ii} - \frac{\sum \chi_{jj}}{3}\right)\right], \tag{S5}$$

and therefore

$$\left[\frac{1}{3}\sum \sigma_{ii}\sum \chi_{jj} - \sum \sigma_{ii}\chi_{ii}\right] = -\sum \sigma_{ii}\left[\left(\chi_{ii} - \frac{\sum \chi_{jj}}{3}\right)\right], \tag{S6}$$

which are identical.

S2 Spectra acquisition and analysis

The spectra were acquired on a Bruker Avance III spectrometer operating at 400 MHz ^{1}H Larmor frequency (9.4 T), equipped with a 5 mm ^{1}H selective probe [2] and on a Bruker Avance NEO spectrometer operating at 1.2 GHz ^{1}H Larmor frequency with a 28.2 T HTS/LTS hybrid magnet,[3] using a 3 mm triple resonance TCI cryo-probehead (for the spectra of the nickel complexes) and a TXO cryo-probehead (for the other complexes). Acquisition was performed with the Bruker TopSpin software and acquisition parameters are reported in table S1. To ensure consistency, the temperature was measured from the chemical shift difference between the -OH and the -CH$_3$ signal of deuterated methanol 99.8% standard sample was performed before each acquisition session. As suggested by Griesinger and co-workers[4], this measure is field-independent, and ensures a ± 0.025 K accuracy.

The following samples were prepared and used for ^{1}H NMR spectra acquisition:

- DyDOTA 5 mM, in D2O + TMSP,
- YbDOTA 5 mM, in D2O + TMSP,
- DyHPDO3A 5 mM, in D2O + TMSP,
- YbHPDO3A 5 mM, in D2O + TMSP,
- NiSAL HDPT 5 mM, in $CDCl_3$,
- NiSAL MeDPT 5 mM, in $CDCl_3$,
- $Co(Tp)_2$ 5 mM, in $CDCl_3$

All the spectra were processed through the application of *qsin* apodization function with SSB = 2, Fourier transformed and phase corrected, using the open-source KLASSEZ package (available at: https://github.com/MetallerTM/klassez). The shift values were extracted from the processed spectra and plotted against temperature using the TRAGICO package [5] (available at https://github.com/letiziafiorucci/tragico). The script used in this procedure is reported in listing S1.

The baseline of cobalt(II), ytterbium(III), and dysprosium(III) spectra at high field (presented in Figure 1 of the main text) were corrected using the fast iterative filtering algorithm[6].

Table S1: Acquisition parameters of NMR spectra with a simple pulse-acquisition (zg) sequence. Recovery delay is the sum of the aquisition time aq, the d1 time delay preceding the acquisition pulse, the dead time DE, and 30 ms disk writing delay. dw is the dwell time. o1p is the carrier frequency.

sample (field)	p1 (μs)	d1 (s)	ν_{nut} (kHz)	dw (μs)	DE (μs)	o1p (ppm)
NiSAL, $Co(Tp)_2$ (400 MHz)	1.0	0.1	55	1.25	5.0	7.28
NiSAL, $Co(Tp)_2$ (1.2 GHz)	0.333	0.06	37	0.4	10.0	7.28
DOTA, HPDO3A (400 MHz)	0.3	0.0197	55	0.9	6.0	4.7
DOTA, HPDO3A (1.2 GHz)	0.333	0.02	27	0.4	10.0	4.7

Listing S1: Code listing for the extraction of chemical shifts from series of monodimensional spectra using TRAGICO collection of functions. This specific example refers to cobalt(II) 400 MHz spectra but the same procedure was applied to all the other experimental spectra. This script also includes the calculation of shifts at 298.0 K and those relative to temperature deviations of ± 0.1 K.

```
from f_fit import *
import os

Tset_meod = np.array([297.0, 297.2, 297.4, 297.6, 297.8, 298.0,
    298.2, 298.4, 298.6, 298.8, 299.0])
Ttrue_meod = np.array([296.35, 296.58, 296.82, 297.04, 297.25,
    297.47, 297.71, 297.89, 298.13, 298.34, 298.56])

fig = plt.figure()
fig.set_size_inches(4.3, 4)
ax = fig.add_subplot(111)
#show grid
```

```
ax.grid(True, linestyle=’--’, linewidth=0.5, color=’gray’, alpha=0.7)
# trend line
m, q = np.polyfit(Tset_meod, Ttrue_meod, 1)
#compute R2
R2 = np.corrcoef(Tset_meod, Ttrue_meod)[0,1]**2
ax.plot(Tset_meod, m*np.array(Tset_meod)+q,’--’, c=’r’, label=’y = {:.2f}x + {:.2f}\nR$^2$ = {:.5f}’.format(m, q, R2))
ax.errorbar(Tset_meod, Ttrue_meod, xerr=0.05, fmt=’none’, yerr=0.05, color=’black’, elinewidth=1, capsize=3)
ax.plot(Tset_meod, Ttrue_meod, ’s’, c=’b’, markersize=4)
ax.set_xlabel(’T$_{set}$ (K)’, fontsize=14)
ax.set_ylabel(’T$_{true}$ (K)’, fontsize=14)
ax.set_xticklabels(ax.get_xticks(), fontsize=11)
ax.set_yticklabels(ax.get_yticks(), fontsize=11)
plt.legend(fontsize=11)
plt.tight_layout()
plt.savefig(’temp_cal.png’, dpi=600)

path = ’path/to/cobalt_at_400MHz/spectra/folder’

num_sp = list(np.arange(10,21,1))
list_sp = [str(i)+’/pdata/1’ for i in num_sp]

# shift (ppm), lw (ppm), x_g (adim.), k (adim.), ph (rad), A-B-C-D-E (a.u.)
lim1 = {’shift’:(-2,2), ’lw’:(1e-4,2.5), ’xg’:(0,0.5), ’B’:(0,0), ’C’:(0,0), ’D’:(0,0), ’E’:(0,0)}
lim2 = {’lw’:(0.7,1.3), ’ph’:(0.9,1.1), ’xg’:(0,0)}


_, _, (shift_tot, shift_tot_err), x, _ = model_fit_1D(
        path,
        Tset_meod,
        list_sp,
        option=1,
        dofit= True,
        fast=True,
        limits1 = lim1,
        limits2 = lim2,
        Param=’shift’)

Tcorr = m*x+q

shift_298 = []
shift_298_1 = []
shift_297_9 = []
for i in range(shift_tot.shape[-1]):

    fig = plt.figure()
    fig.set_size_inches(5, 4)
    ax = fig.add_subplot(111)
    ax.grid(True, linestyle=’--’, linewidth=0.5, color=’gray’, alpha=0.7)
    m, q = np.polyfit(1/Tcorr, shift_tot[:,i], 1)
    R2 = np.corrcoef(1/Tcorr, shift_tot[:,i])[0,1]**2
    ax.plot(1/Tcorr, m*(1/Tcorr)+q,’--’, c=’r’, label=’y = {:.2f}x + {:.2f}\nR$^2$ = {:.5f}’.format(m, q, R2))
    xerr = 0.1/Tcorr*(1/Tcorr)
```

```
    ax.errorbar(1/Tcorr, shift_tot[:,i], xerr=xerr, fmt='none', yerr
        =np.abs(shift_tot_err[:,i]), color='black', elinewidth=1,
        capsize=3)
    ax.plot(1/Tcorr, shift_tot[:,i], 's', c='b', markersize=4)
    ax.set_xlabel('1/T$_{corr}$ (K$^{-1}$)', fontsize=14)
    plt.xticks(rotation=45)
    ax.set_ylabel('Shift (ppm)', fontsize=14)
    ax.tick_params(labelsize=11)
    plt.legend(fontsize=11)
    plt.tight_layout()
    plt.savefig('shift_cal_400_'+str(i)+'.png', dpi=600)
    plt.show()

    shift_298.append(m*(1/298)+q)
    shift_298_1.append(m*(1/298.1)+q)
    shift_297_9.append(m*(1/297.9)+q)

print(np.array(shift_298))
print(np.array(shift_298_1))
print(np.array(shift_297_9))
#end
```

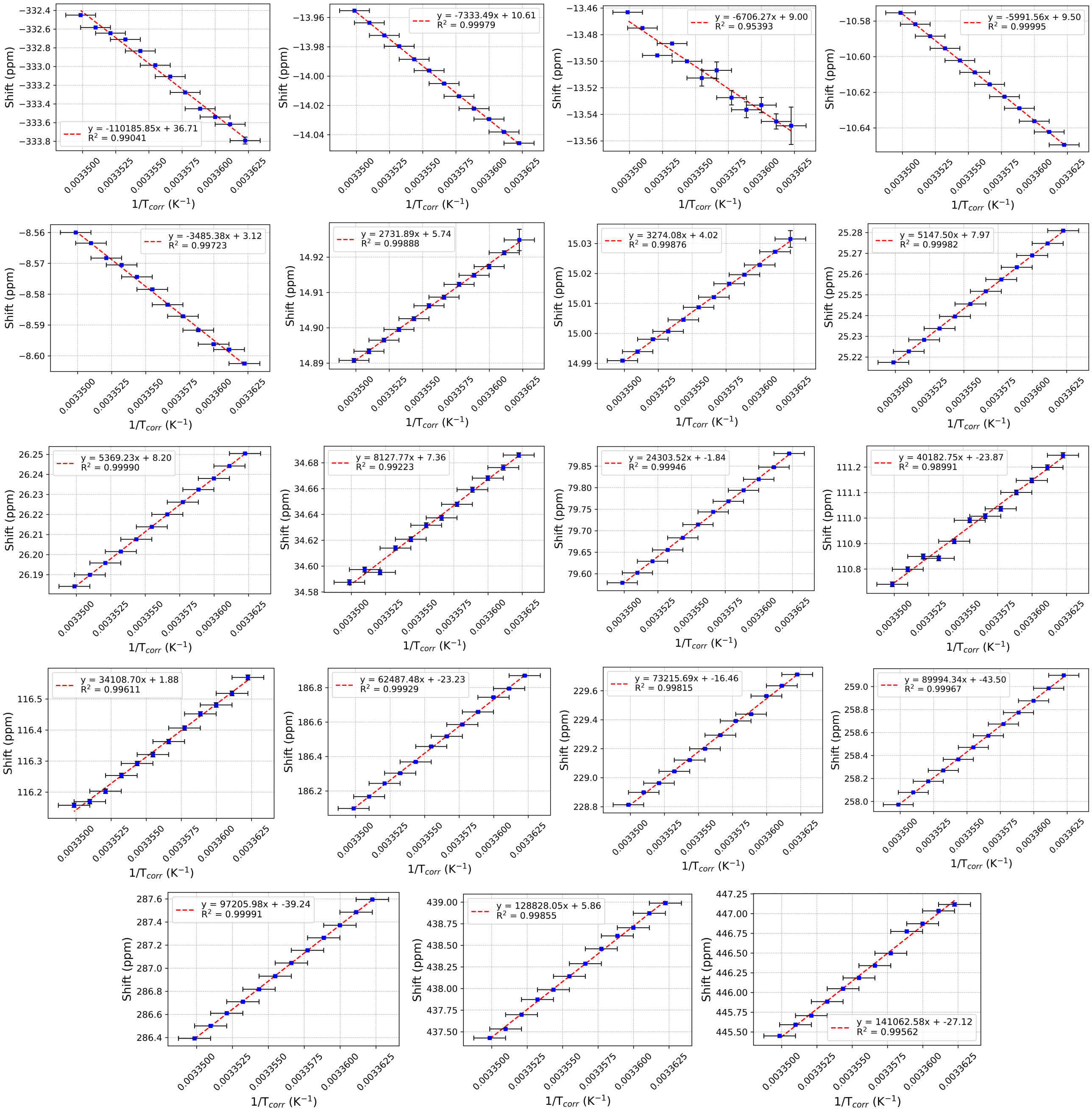

Figure S1: Temperature dependence of NiSAL-HDPT peaks extracted with TRAGICO (see listing S1) for spectra acquired at 400 MHz ^1H Larmor frequency. The temperature values on the x-axis were corrected (T_{corr}) using the calibration procedure (*vide infra*).

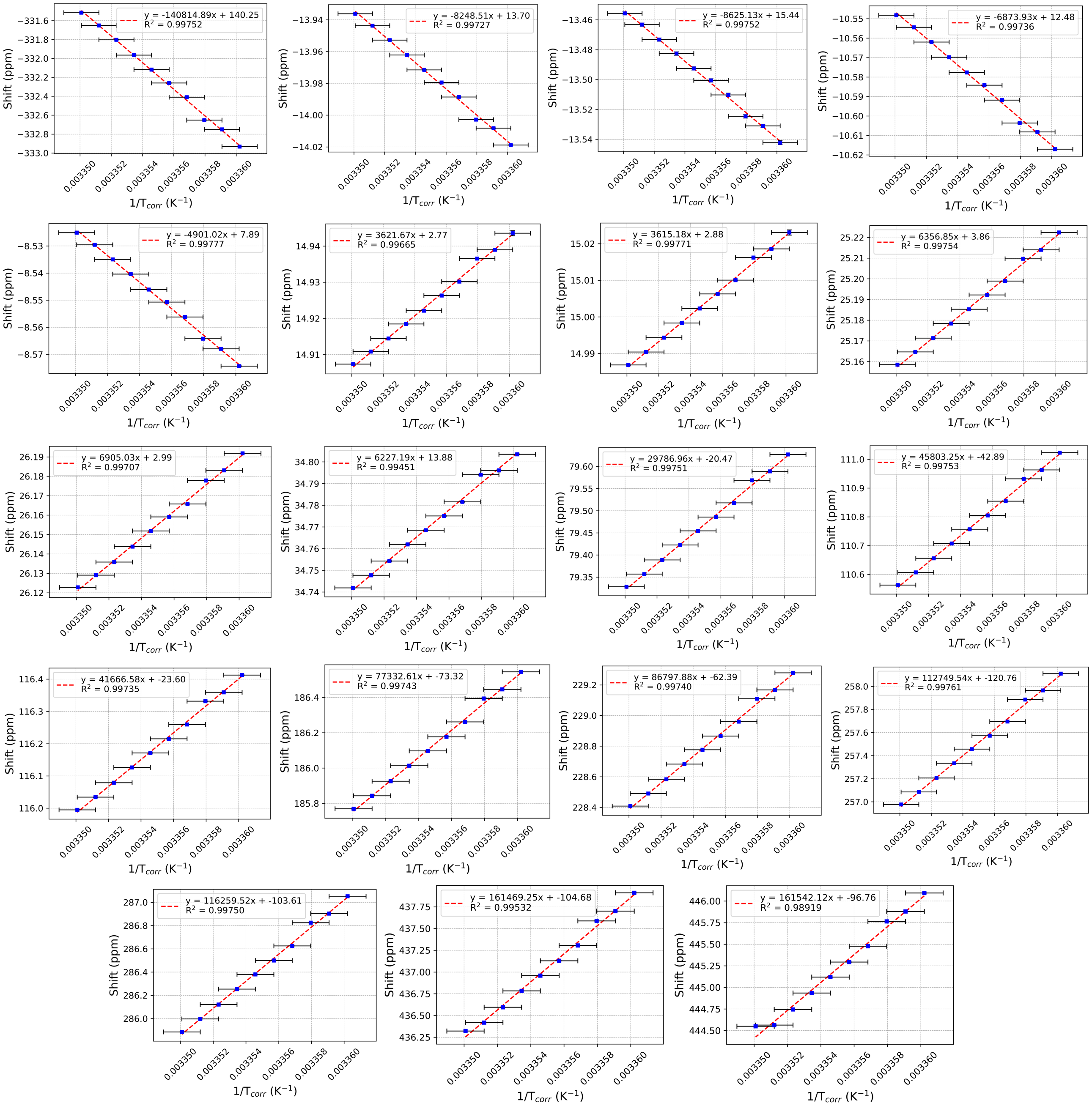

Figure S2: Temperature dependence of NiSAL-HDPT peaks extracted with TRAGICO (see listing S1) for spectra acquired at 1200 MHz ^1H Larmor frequency. The temperature values on the x-axis were corrected (T_{corr}) using the calibration procedure (*vide infra*).

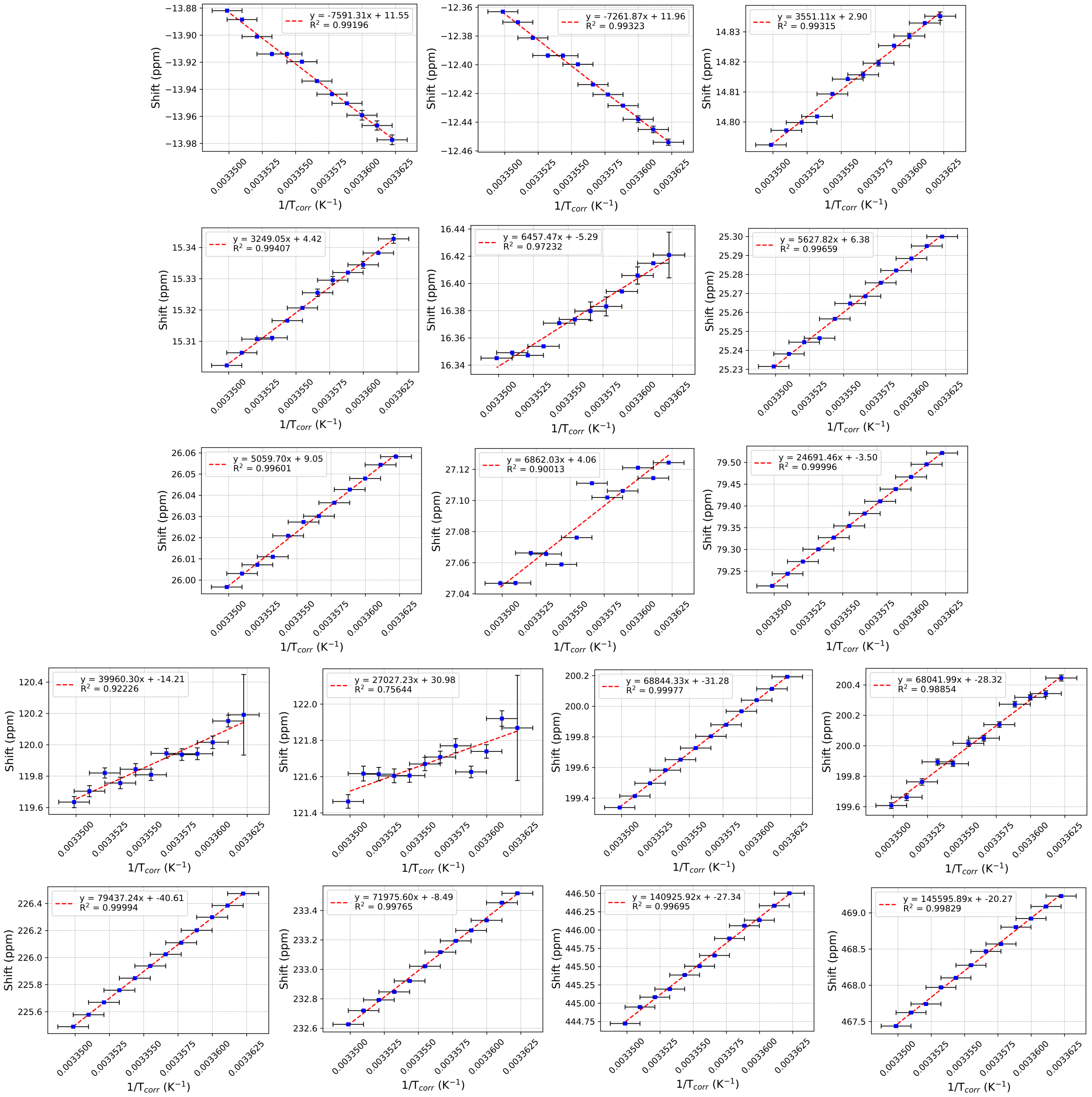

Figure S3: Temperature dependence of NiSAL-MeDPT peaks extracted with TRAGICO (see listing S1) for spectra acquired at 400 MHz ^{1}H Larmor frequency. The temperature values on the x-axis were corrected (T_{corr}) using the calibration procedure (*vide infra*).

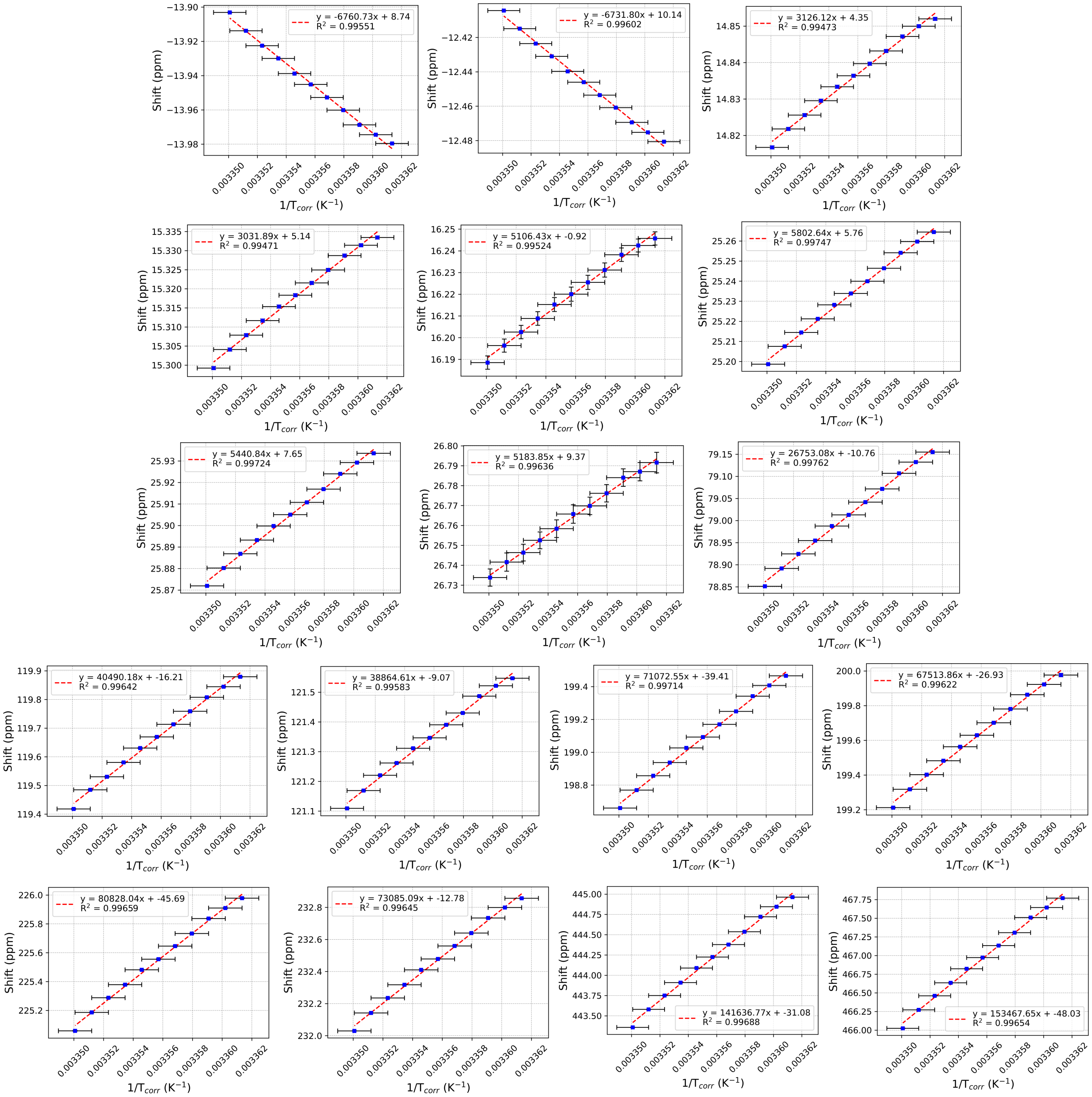

Figure S4: Temperature dependence of NiSAL-MeDPT peaks extracted with TRAGICO (see listing S1) for spectra acquired at 1200 MHz ^1H Larmor frequency. The temperature values on the x-axis were corrected (T_{corr}) using the calibration procedure (*vide infra*).

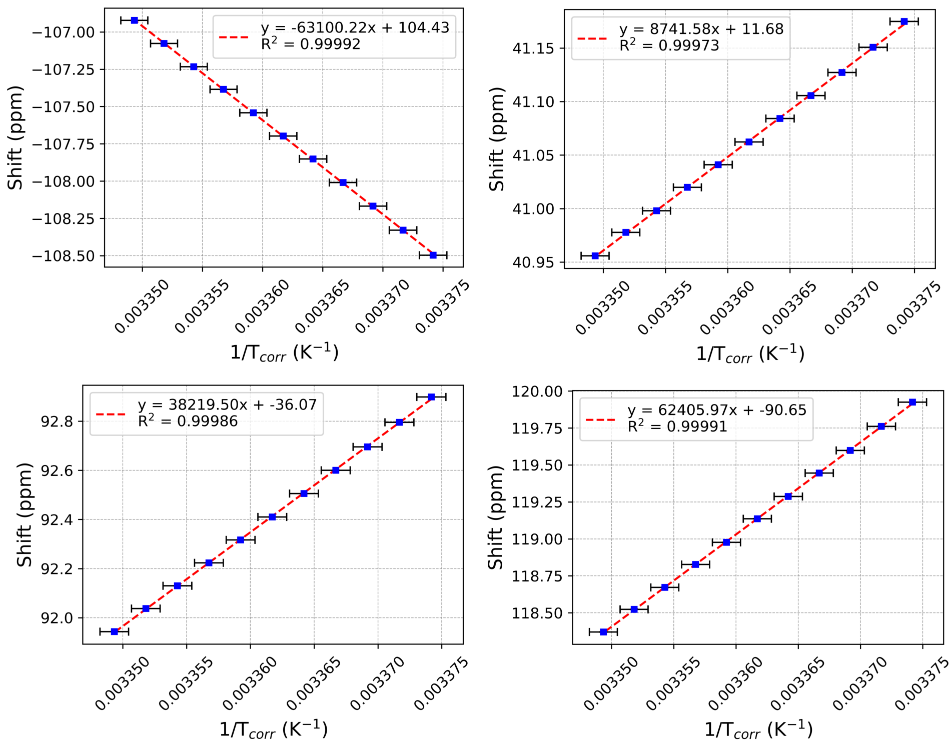

Figure S5: Temperature dependence of CoTp$_2$ peaks extracted with TRAGICO (see listing S1) for spectra acquired at 400 MHz ^1H Larmor frequency. The temperature values on the x-axis were corrected (T_{corr}) using the calibration procedure (*vide infra*).

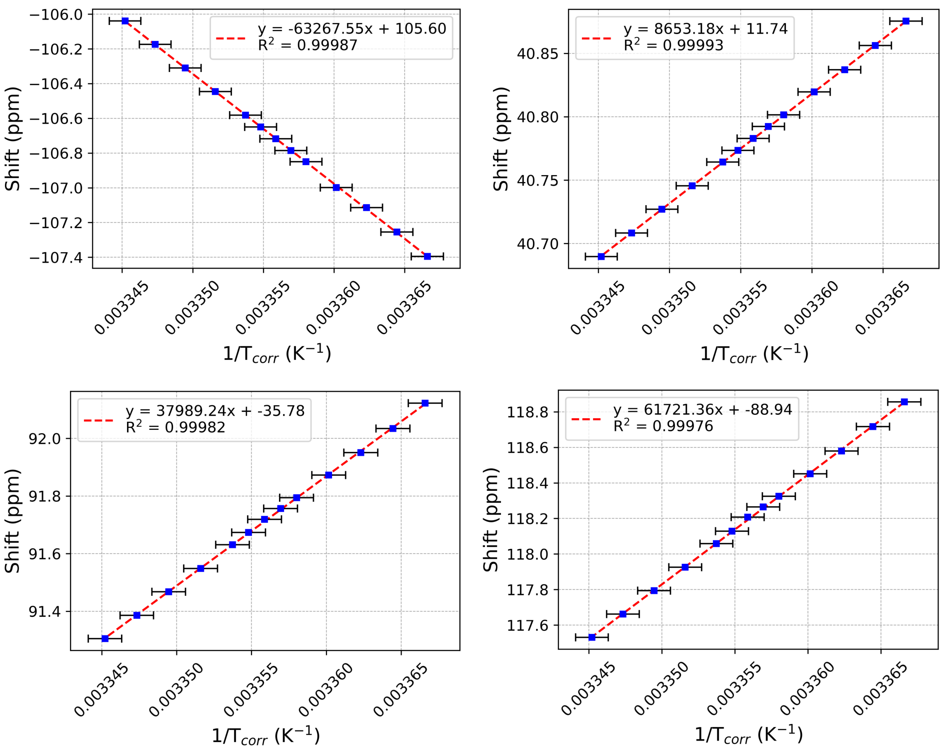

Figure S6: Temperature dependence of CoTp$_2$ peaks extracted with TRAGICO (see listing S1) for spectra acquired at 1200 MHz ^1H Larmor frequency. The temperature values on the x-axis were corrected (T_{corr}) using the calibration procedure (*vide infra*).

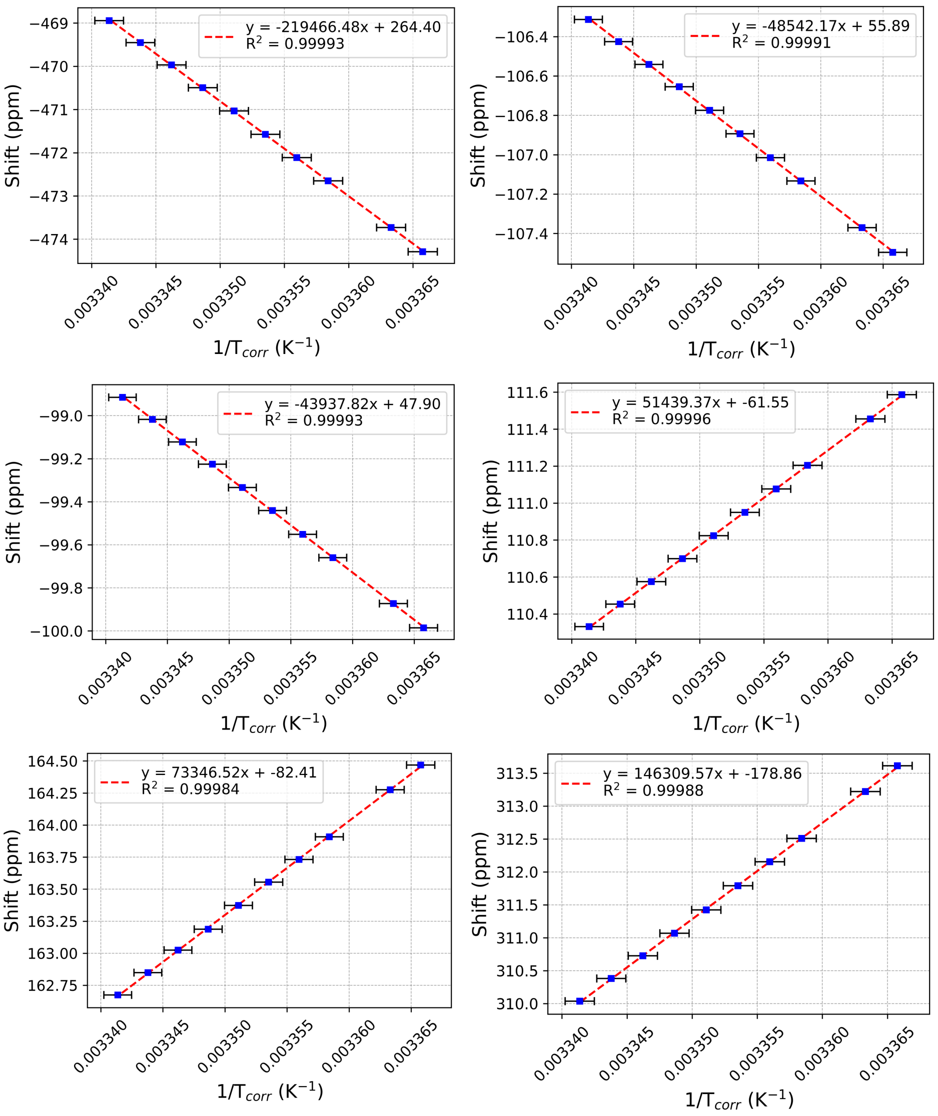

Figure S7: Temperature dependence of DyDOTA SAP peaks extracted with TRAGICO (see listing S1) for spectra acquired at 400 MHz ^1H Larmor frequency. The temperature values on the x-axis were corrected (T_{corr}) using the calibration procedure (*vide infra*).

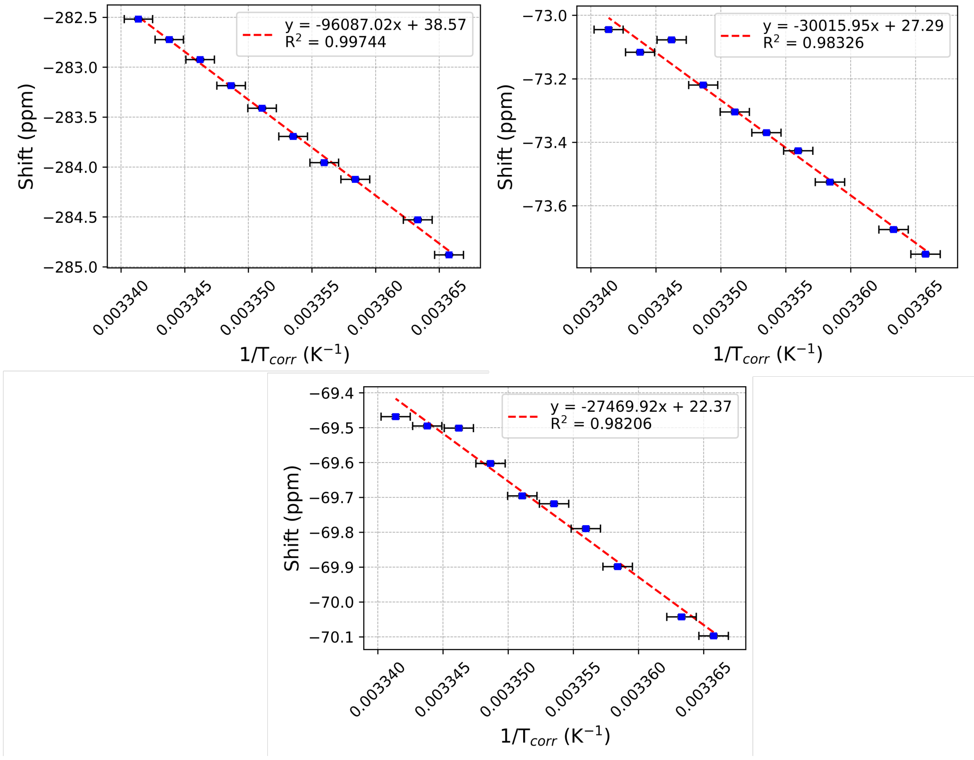

Figure S8: Temperature dependence of DyDOTA TSAP peaks extracted with TRAGICO (see listing S1) for spectra acquired at 400 MHz ^1H Larmor frequency. The temperature values on the x-axis were corrected (T_{corr}) using the calibration procedure (*vide infra*).

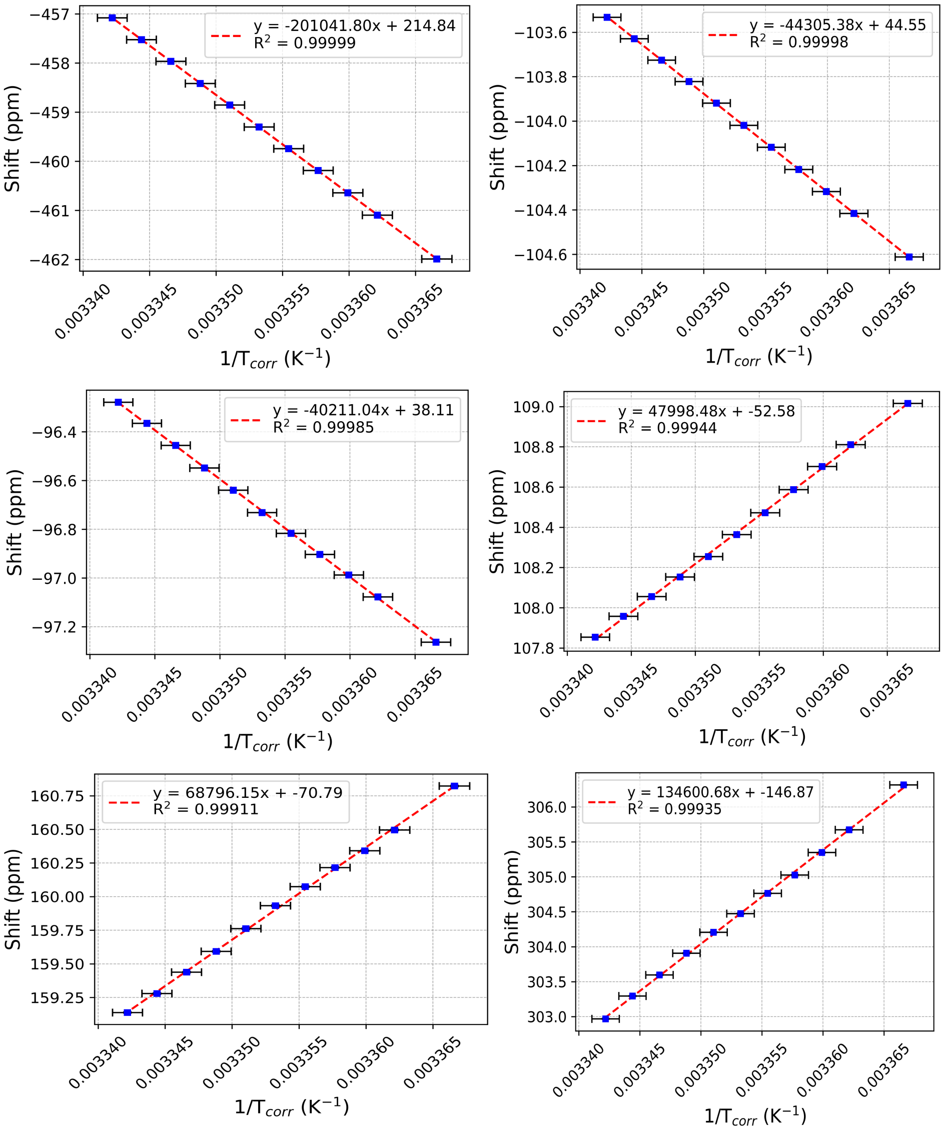

Figure S9: Temperature dependence of DyDOTA SAP peaks extracted with TRAGICO (see listing S1) for spectra acquired at 1200 MHz ^1H Larmor frequency. The temperature values on the x-axis were corrected (T_{corr}) using the calibration procedure (*vide infra*).

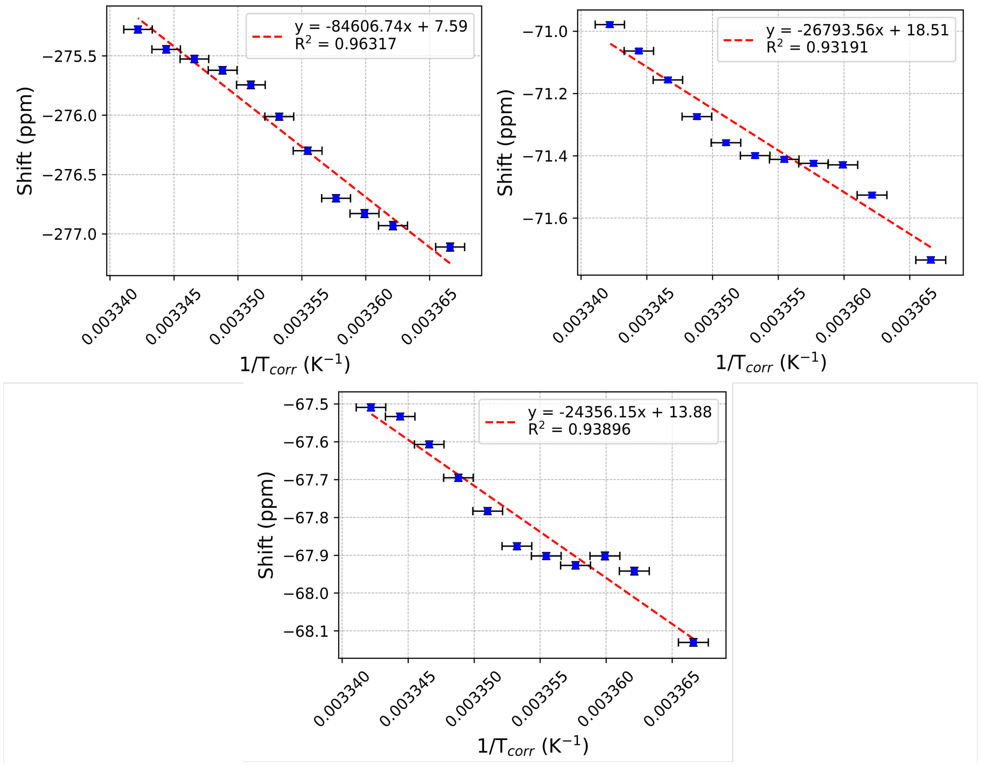

Figure S10: Temperature dependence of DyDOTA TSAP peaks extracted with TRAGICO (see listing S1) for spectra acquired at 1200 MHz ^{1}H Larmor frequency. The temperature values on the x-axis were corrected (T_{corr}) using the calibration procedure (*vide infra*).

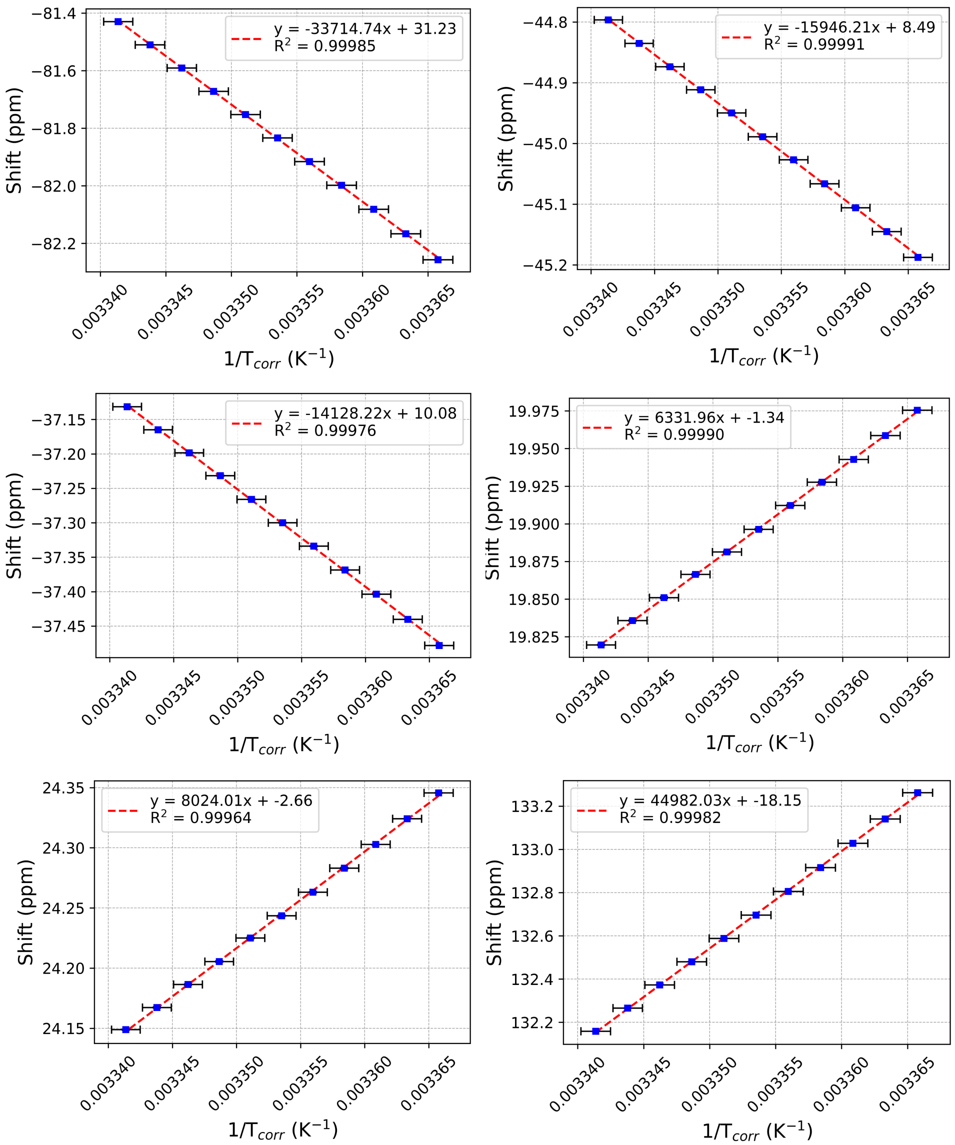

Figure S11: Temperature dependence of YbDOTA SAP peaks extracted with TRAGICO (see listing S1) for spectra acquired at 400 MHz ^{1}H Larmor frequency. The temperature values on the x-axis were corrected (T_{corr}) using the calibration procedure (*vide infra*).

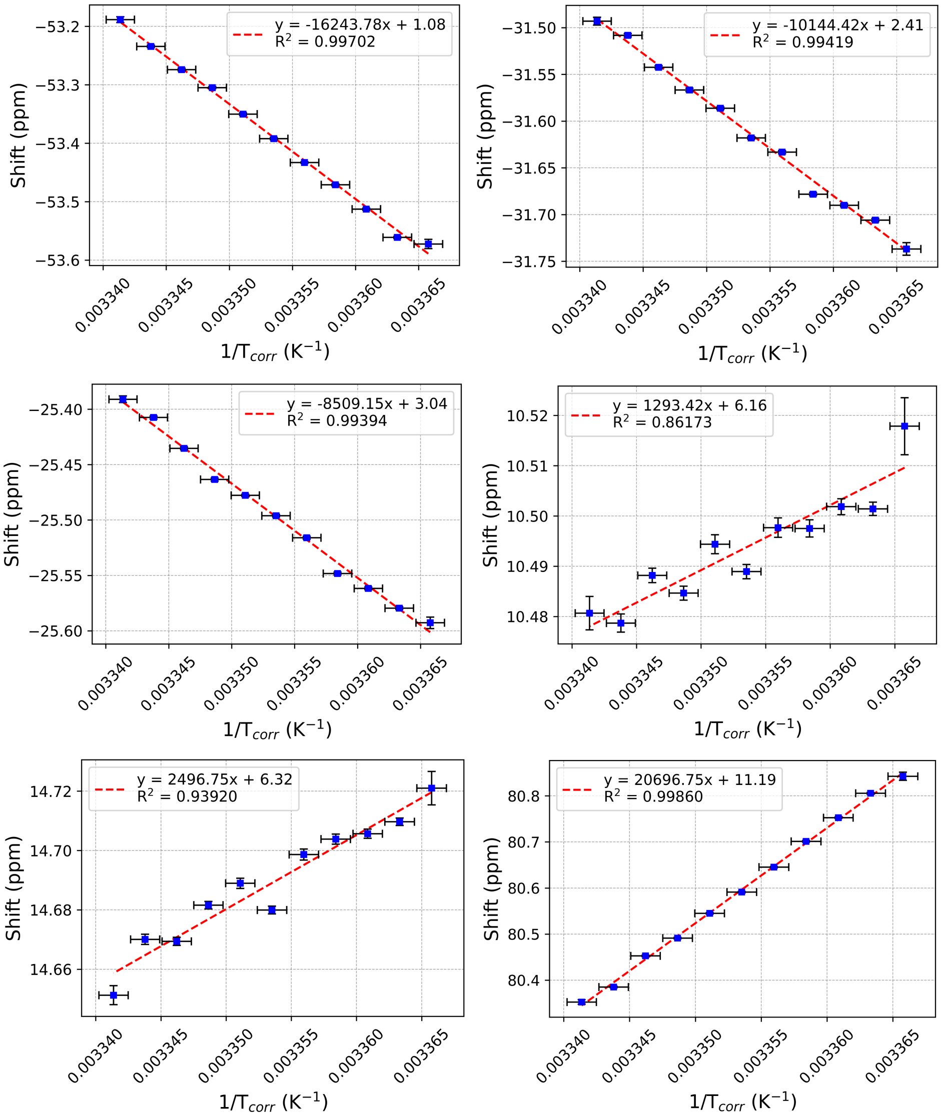

Figure S12: Temperature dependence of YbDOTA TSAP′ peaks extracted with TRAGICO (see listing S1) for spectra acquired at 400 MHz ^1H Larmor frequency. The temperature values on the x-axis were corrected (T_{corr}) using the calibration procedure (*vide infra*).

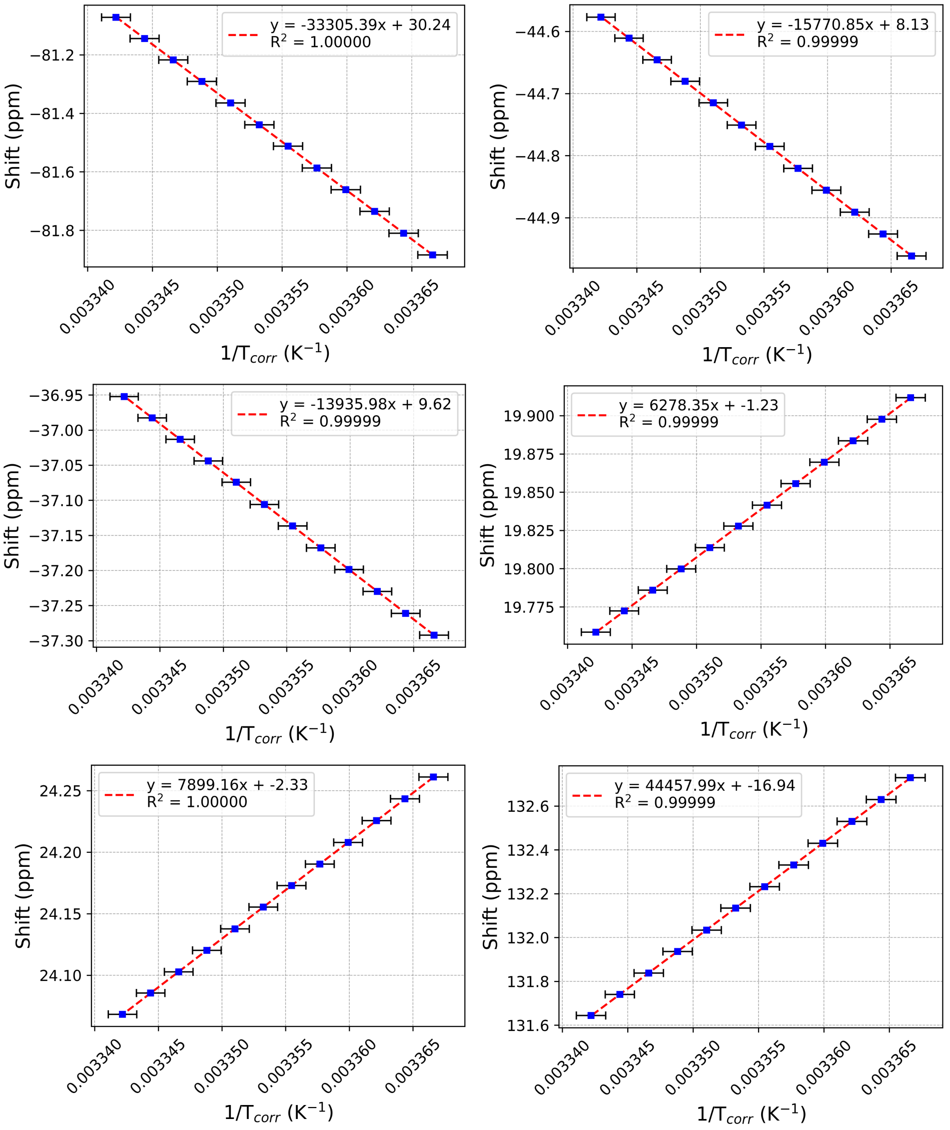

Figure S13: Temperature dependence of YbDOTA SAP peaks extracted with TRAGICO (see listing S1) for spectra acquired at 1200 MHz ^{1}H Larmor frequency. The temperature values on the x-axis were corrected (T_{corr}) using the calibration procedure (*vide infra*).

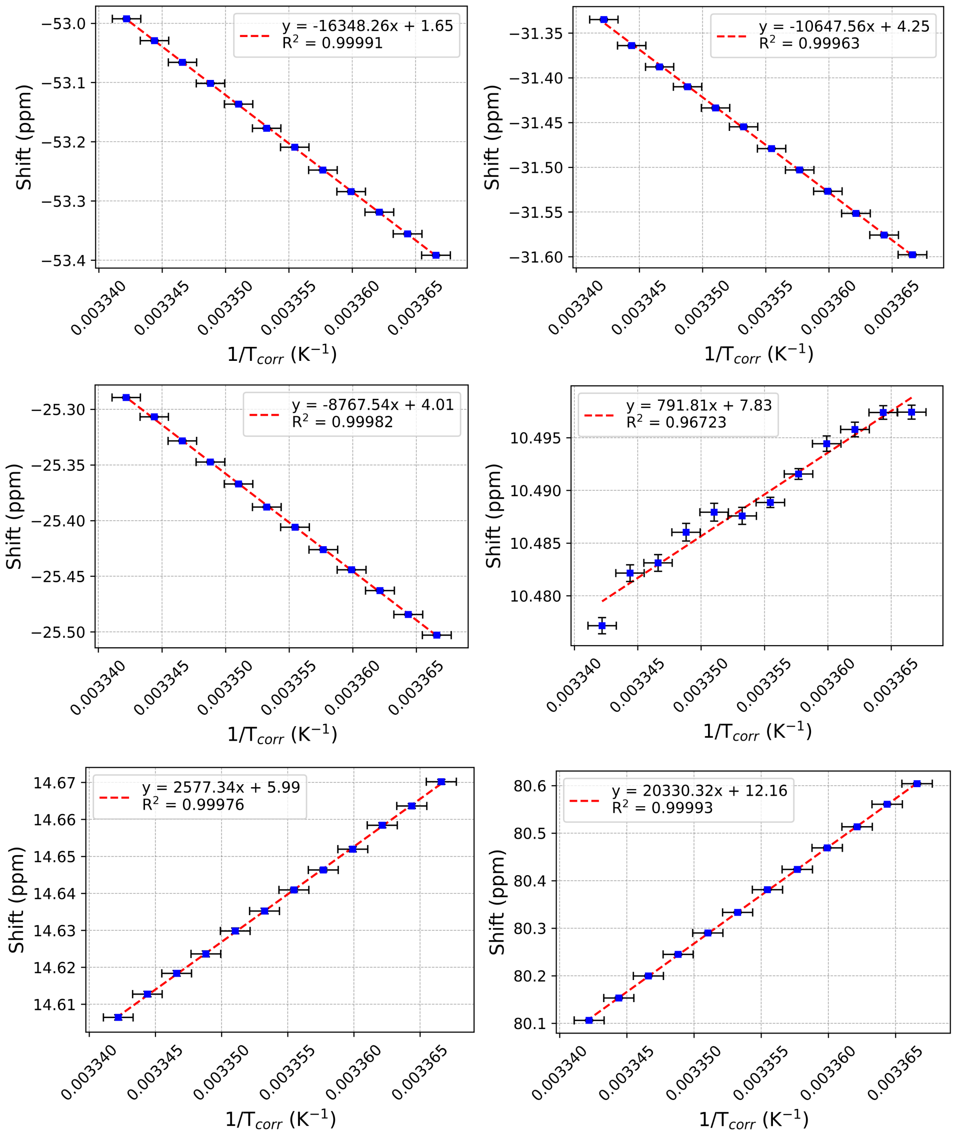

Figure S14: Temperature dependence of YbDOTA TSAP′ peaks extracted with TRAGICO (see listing S1) for spectra acquired at 1200 MHz ^1H Larmor frequency. The temperature values on the x-axis were corrected (T_{corr}) using the calibration procedure (*vide infra*).

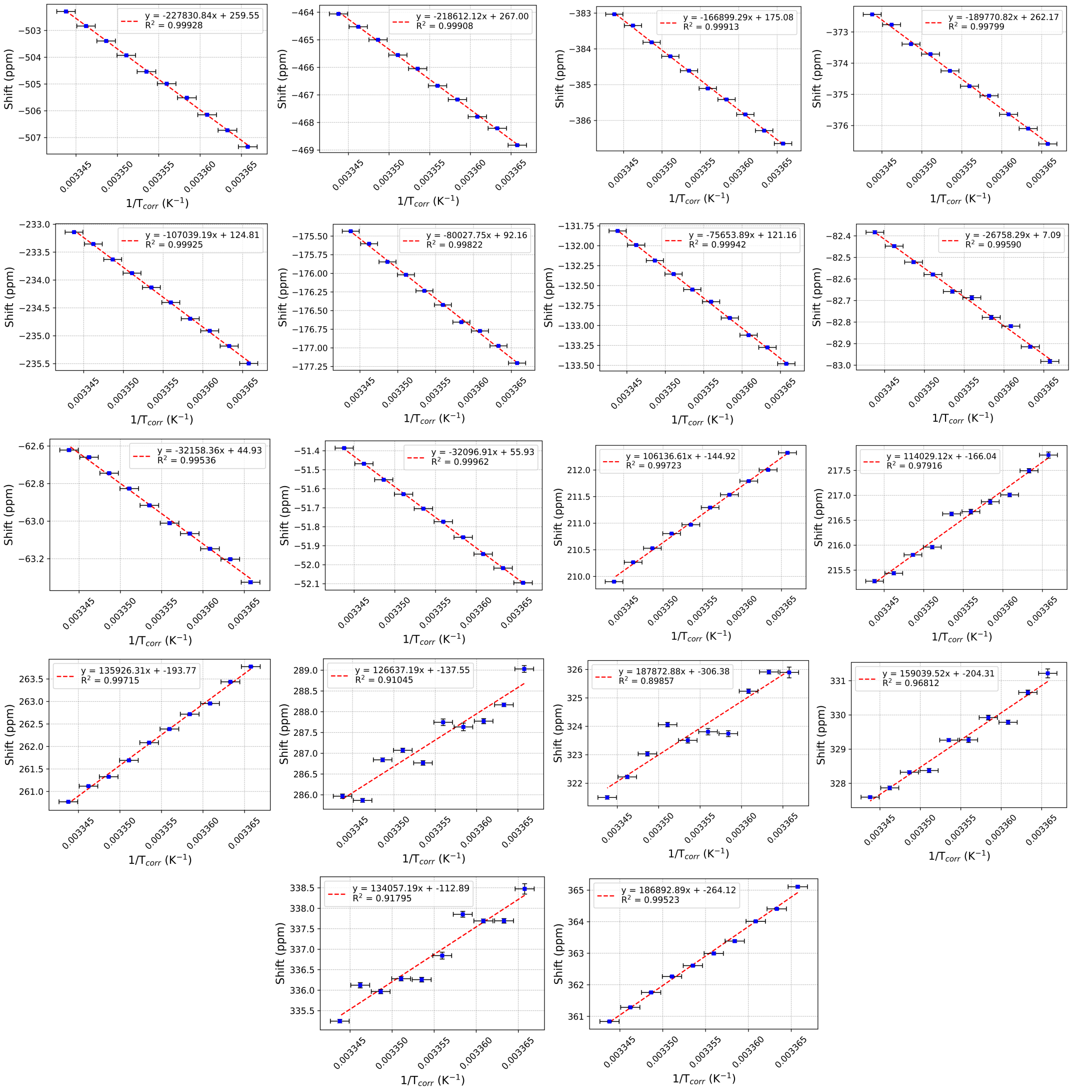

Figure S15: Temperature dependence of DyHPDO3A peaks extracted with TRAGICO (see listing S1) for spectra acquired at 400 MHz ^1H Larmor frequency. The temperature values on the x-axis were corrected (T_{corr}) using the calibration procedure (*vide infra*).

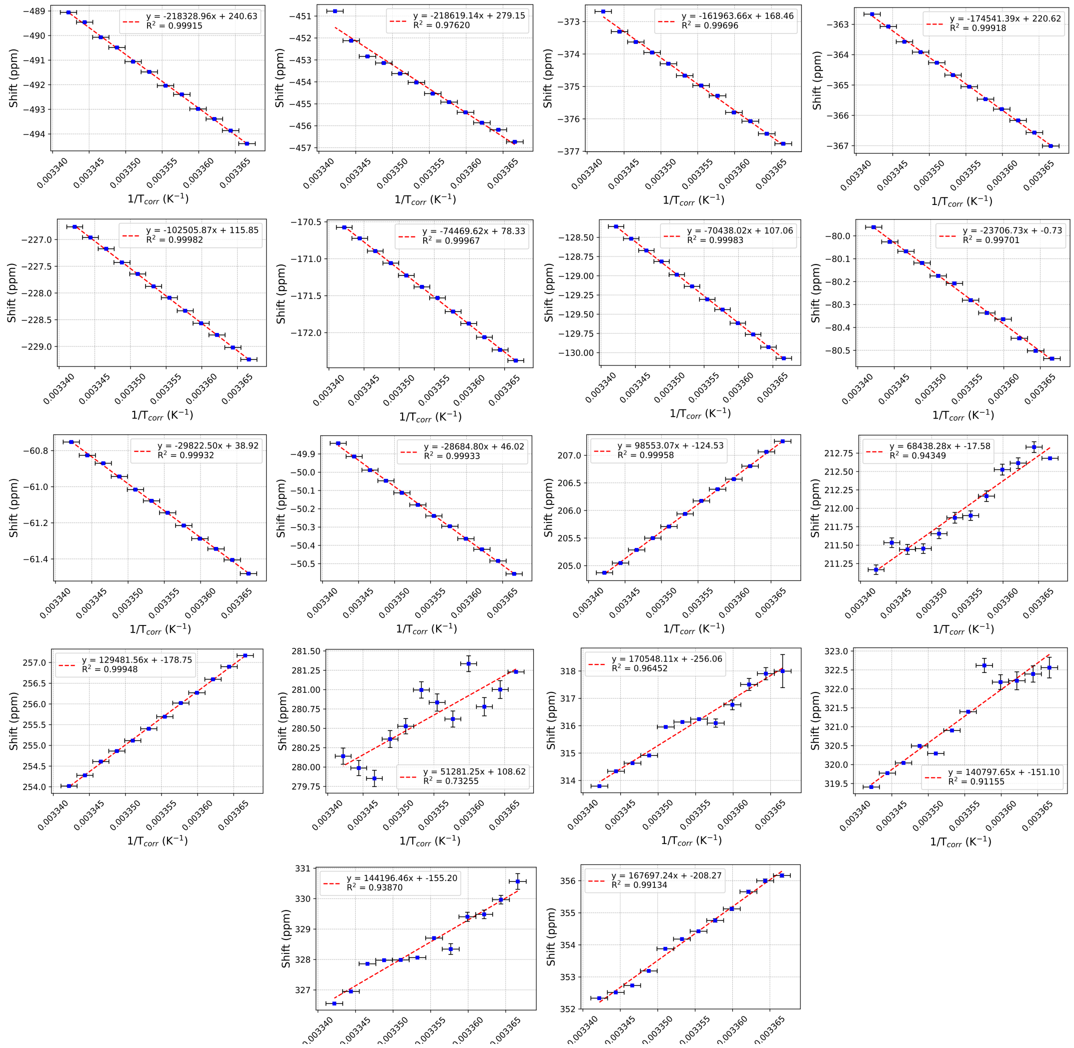

Figure S16: Temperature dependence of DyHPDO3A peaks extracted with TRAGICO (see listing S1) for spectra acquired at 1200 MHz ^1H Larmor frequency. The temperature values on the x-axis were corrected (T_{corr}) using the calibration procedure (*vide infra*).

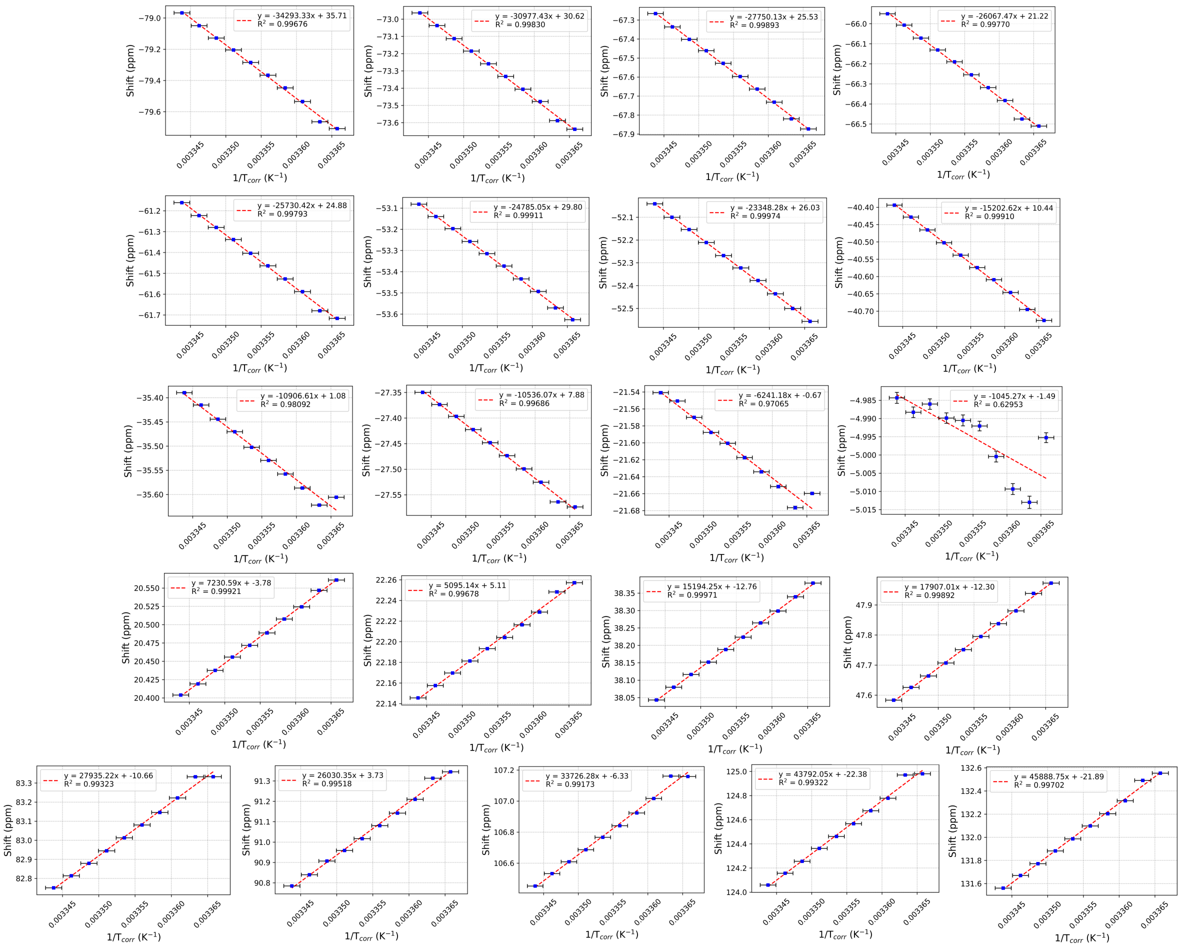

Figure S17: Temperature dependence of YbHPDO3A peaks extracted with TRAGICO (see listing S1) for spectra acquired at 400 MHz ^1H Larmor frequency. The temperature values on the x-axis were corrected (T_{corr}) using the calibration procedure (*vide infra*).

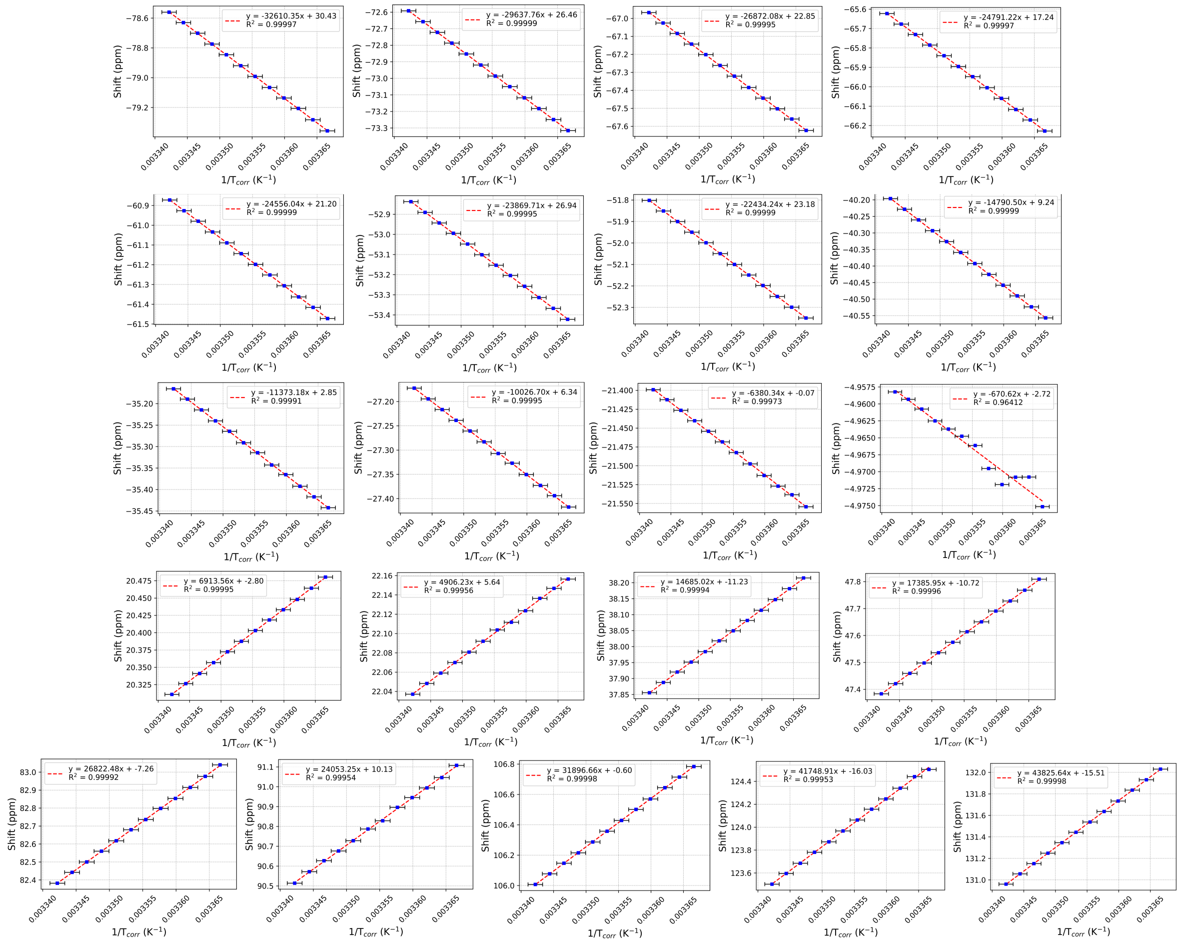

Figure S18: Temperature dependence of YbHPDO3A peaks extracted with TRAGICO (see listing S1) for spectra acquired at 1200 MHz ^{1}H Larmor frequency. The temperature values on the x-axis were corrected (T_{corr}) using the calibration procedure (*vide infra*).

S3 HPDO3A assignment

The assignment of HPDO3A signals was carried out for both the dysprosium and ytterbium complexes using a Monte Carlo algorithm with simulated annealing, with the goal of minimizing the difference between simulated and experimental shifts by iteratively swapping coordinate indices, calculating the susceptibility (χ) via a linear system using the reordered coordinates and the experimental shifts, and then recalculating, through the inverse linear system, the shifts using this new χ tensor. The target is given by the sum of squared differences between experimental and calculated shifts. The simulated shifts also include the diamagnetic contribution, computed with ORCA software v6 on the yttrium analogue of the two conformers SAP and TSAP', with TPSSh functional, Grimme dispersion correction D3BJ, the triple-ζ def2-TZVP basis set, RIJCOSX approximation (applied also to GIAO integrals with dedicated flag) with def2/J and def2-TZVP/C auxiliary basis sets and tighter grid settings (DefGrid3), NoFrozenCore option and CPCM implicit solvent model for water.

The pseudocode for this procedure is reported as Algorithm 1.

For the dysprosium case, the experimental data corresponds to the chemical shifts values extracted from the monodimensional spectra at a certain temperature. The starting order of coordinates is defined using the ab initio-computed susceptibility tensor at the same temperature. The final coordinates ordering, i.e. the final assignment, is the one corresponding to q_{best}. The coordinates used correspond to the model SAP1-S (according to the nomenclature in [7]), the most abundant in solution, optimized at DFT level (as described in the main text). The agreement between simulated (and adjusted) chemical shifts with experimental data is good (see Figure S19). The assignment is reported in figure S23.

The ytterbium case is more complex since in this case also the minor conformer, TSAP1', is present in non-negligible amount in solution. The algorithm in this case was hence modified to accommodate the EXSY data, with two separate targets computed for the coordinates and shifts of each conformer. The experimental shifts were assigned to one of the two conformers through visual inspection of the peaks' linewidth. The two structural models used correspond to the conformers SAP1-S and (TSAP1-R)' (where the prime indicates the absence of the apical water molecule as ninth ligand). Starting from the order dictated by the ab initio computed χ tensor, the final agreement after optimization between calculated and experimental shifts is very good (see Figures S20 and S21). The assignment is reported in figure S22.

The susceptibility tensors computed ab initio for the different HPDO3A analogues and the corresponding tensors computed from the experimental values after adjustment with algorithm 1 are reported in Table S2.

Algorithm 1 Assignment via Monte-Carlo algorithm

```
function TARGET_COMPUTATION(coordinates, order, experimental_shifts)
    coordinates_sorted = coordinates[order]
    $\chi$ = (coordinates_sorted)$^{-1}$ · experimental_shifts
    simulated_shifts = coordinates_sorted · $\chi$
    $q = \sum$(simulated_shifts − experimental_shifts)$^2$
    return $q$
end function

$T_0$ = starting temperature
$q_{\text{best}} = \infty$
for all cycle do
    $T$ = reduced_temperature($T_0$)
    order = new ordering
    $q$ = TARGET_COMPUTATION(coordinates, order, experimental_shifts)
    $\Delta E = q_t - q$
    $\Delta E/T = -\Delta E/T$
    if exp($\Delta E/T$) > random_number(0,1) then
        $q_t = q$
    end if
    if $q < q_{\text{best}}$ then
        $q_{\text{best}} = q$
    end if
end for
```

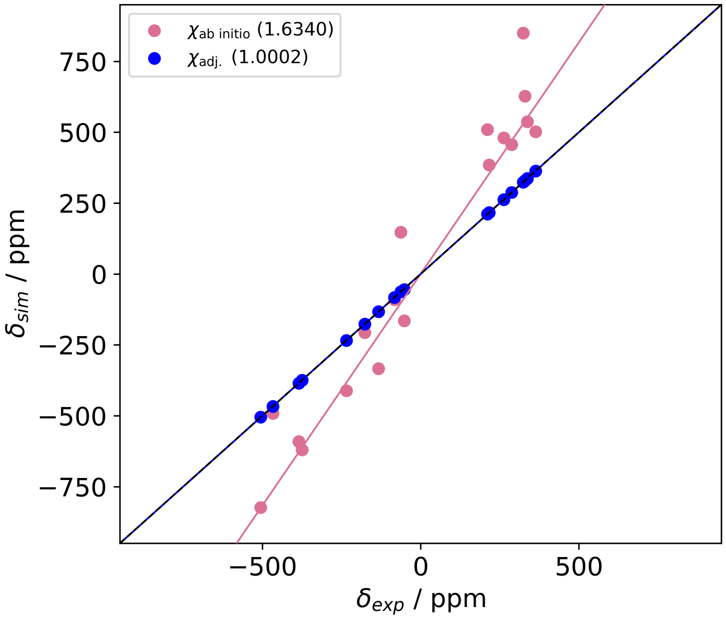

Figure S19: Scatter plot of simulated and experimental chemical shifts of DyHPDO3A extracted from monodimensional spectrum at 400 MHz 1H Larmor frequency at 298.0 K. The two sets of points refer to simulated PC shifts for SAP conformer of DyHPDO3A from the χ tensor computed ab initio with protocol 2 (section S4), $\chi_{\text{ab initio}}$, and from the χ tensor adjusted during the assignment procedure and back-calculated from the experimental shifts, $\chi_{\text{adj.}}$. The complete tensors are reported in Table S2.

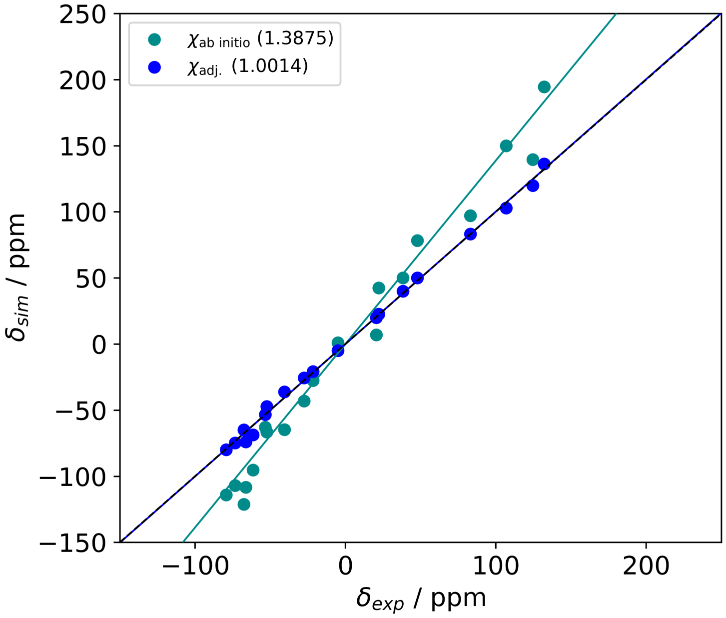

Figure S20: Scatter plot of simulated and experimental chemical shifts of YbHPDO3A extracted from monodimensional spectrum at 400 MHz 1H Larmor frequency at 298.0 K. The two sets of points refer to simulated PC shifts for SAP conformer of YbHPDO3A from the χ tensor computed ab initio with protocol 2 (section S4), $\chi_{\text{ab initio}}$, and from the χ tensor adjusted during the assignment procedure and back-calculated from the experimental shifts, $\chi_{\text{adj.}}$. The complete tensors are reported in Table S2.

$\chi_{\text{ab initio}} \times 10^{-30}$			$\chi_{\text{adj.}} \times 10^{-30}$		
DyHPDO3A (SAP)					
1.481	-0.330	0.041	1.869	-0.245	-0.018
-0.330	0.579	-0.535	-0.245	0.121	-0.278
0.041	-0.535	0.890	-0.018	-0.278	0.960
YbHPDO3A (SAP)					
0.370	0.065	0.044	0.360	0.053	0.028
0.065	-0.036	0.088	0.053	-0.011	0.058
0.044	0.088	0.185	0.028	0.058	0.171
YbHPDO3A (TSAP’)					
0.119	0.023	0.079	0.283	0.008	0.028
0.023	0.154	0.077	0.008	0.052	0.039
0.079	0.077	0.222	0.028	0.039	0.185

Table S2: Magnetic susceptibility tensors in m^3 of DyHPDO3A conformed SAP and YbHPDO3A conformers SAP and TSAP’ ($\chi_{\text{ab initio}}$) simulated ab initio with protocol (2) (see section S4) and computed from experimental shifts ($\chi_{\text{adj.}}$), at 298.0 K.

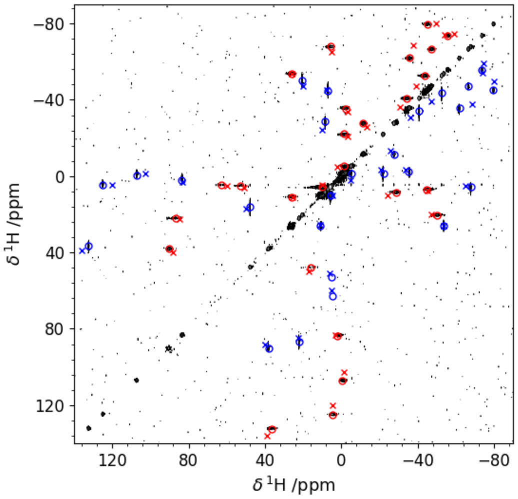

Figure S21: Experimental ^{1}H-^{1}H EXSY spectrum of YbHPDO3A. The cross represent the simulated chemical shifts after MC-adjustment and the circles the experimental shift values used in the procedure. The symbols are reported in red for SAP conformer and blue for TSAP′ conformer.

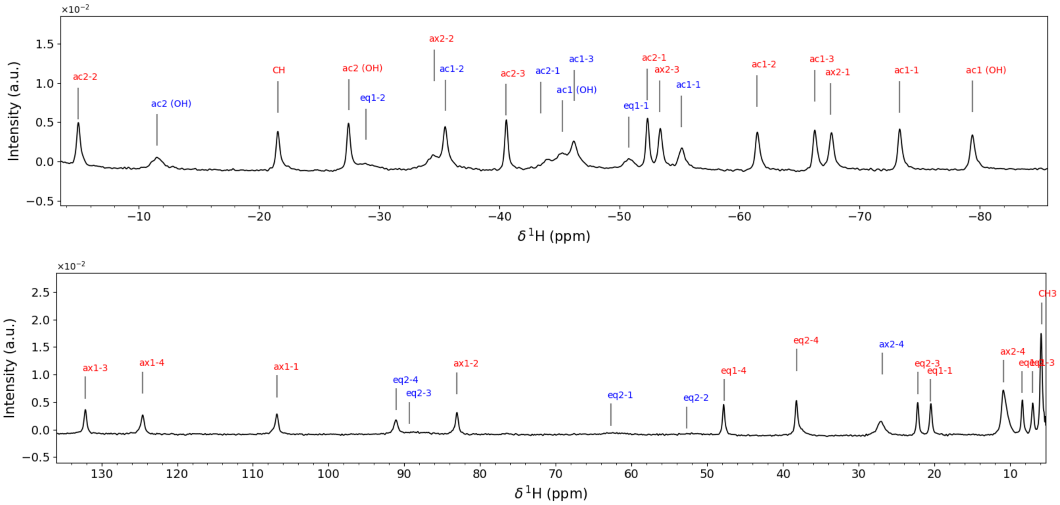

Figure S22: Peak assignment of YbHPDO3A made using algorithm 1. In red the labels refer to the SAP conformer and the blue to the TSAP′ conformer. The labels correspond to the positions in the structure of figure S37 and the number after − indicates the replica number (in progressive number in agreement with the position in the XYZ file).

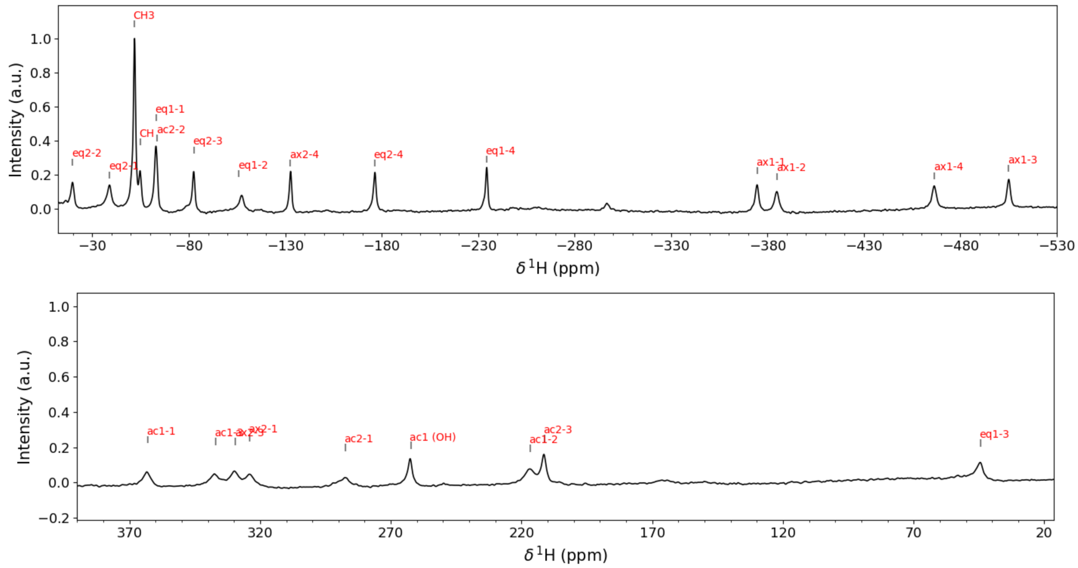

Figure S23: Peak assignment of DyHPDO3A made using algorithm 1. In red the labels refer to the SAP conformer. The labels correspond to the positions in the structure of figure S37 and the number after − indicates the replica number (in progressive number in agreement with the position in the XYZ file).

label	$\delta_{\mathrm{exp},400}$	$\delta_{\mathrm{exp},1200}$	$\Delta\delta_{\mathrm{exp}}$	$\Delta\delta_{\mathrm{exp}}^{\mathrm{rel}} \times 100$
NH	-333.045	-332.284	0.761	-0.229
3	-13.998	-13.981	0.017	-0.123
3′	-13.509	-13.502	0.006	-0.046
$\beta_1{}'$	-10.610	-10.586	0.025	-0.232
$\beta_2{}'$	-8.580	-8.552	0.028	-0.330
6′	14.906	14.927	0.020	0.137
6	15.009	15.007	-0.003	-0.018
4′	25.247	25.193	-0.054	-0.213
4	26.215	26.160	-0.055	-0.211
$\alpha_1{}'$	34.632	34.776	0.144	0.415
α_2	79.718	79.491	-0.227	-0.285
$\gamma_2{}'$	110.975	110.812	-0.163	-0.147
γ_2	116.337	116.222	-0.116	-0.099
$\gamma_1{}'$	186.463	186.190	-0.272	-0.146
γ_1	229.231	228.881	-0.350	-0.153
$\alpha_2{}'$	258.495	257.592	-0.903	-0.349
α_1	286.956	286.519	-0.437	-0.152
CH	438.171	437.162	-1.009	-0.230
CH′	446.243	445.332	-0.911	-0.204

Table S3: Experimental shifts extracted in ppm at 298.00 K for NiSAL-HDPT (see figure S25).

label	$\delta_{\text{exp},400}$	$\delta_{\text{exp},1200}$	$\Delta\delta_{\text{exp}}$	$\Delta\delta^{\text{rel}}_{\text{exp}} \times 100$
3	-13.927	-13.944	-0.018	0.128
3′	-12.406	-12.445	-0.039	0.317
6	14.813	14.836	0.023	0.154
6′	15.321	15.318	-0.004	-0.023
$\alpha_1{}'$	16.376	16.219	-0.156	-0.956
4′	25.264	25.233	-0.031	-0.121
4	26.026	25.905	-0.122	-0.467
α_2	27.084	26.764	-0.320	-1.182
CH_3	79.361	79.012	-0.349	-0.440
$\gamma_2{}'$	119.882	119.665	-0.217	-0.181
γ_2	121.674	121.345	-0.330	-0.271
$\gamma_1{}'$	199.743	199.089	-0.655	-0.328
$\alpha_2{}'$	200.010	199.623	-0.387	-0.194
α_1	225.954	225.550	-0.404	-0.179
γ_1	233.042	232.473	-0.570	-0.244
CH	445.568	444.213	-1.355	-0.304
CH′	468.302	466.959	-1.344	-0.287

Table S4: Experimental shifts extracted in ppm at 298.00 K for NiSAL-MeDPT (see figure S25).

label	$\delta_{\text{exp},400}$	$\delta_{\text{exp},1200}$	$\Delta\delta_{\text{exp}}$	$\Delta\delta^{\text{rel}}_{\text{exp}} \times 100$
B	118.762	118.181	-0.581	-0.489
5	92.184	91.706	-0.478	-0.519
4	41.011	40.781	-0.230	-0.560
3	-107.321	-106.705	0.615	-0.573

Table S5: Experimental shifts in ppm extracted at 298.00 K for $CoTp_2$ (see figure S26).

label	$\delta_{\mathrm{exp},400}$	$\delta_{\mathrm{exp},1200}$	$\Delta\delta_{\mathrm{exp}}$	$\Delta\delta^{\mathrm{rel}}_{\mathrm{exp}} \times 100$
		SAP		
ax1	-472.061	-459.797	12.264	-2.598
eq2	-107.003	-104.129	2.873	-2.685
eq1	-99.540	-96.824	2.716	-2.729
ac2	111.065	108.492	-2.573	-2.317
ax2	163.717	160.072	-3.646	-2.227
ac1	312.116	304.808	-7.307	-2.341
		TSAP		
ax1	-283.8731	-276.3261	7.547	-2.659
eq2	-73.4384	-71.4016	2.037	-2.773
eq1	-69.8107	-67.8554	1.955	-2.801

Table S6: Experimental shifts in ppm extracted at 298.00 K for DyDOTA(see figure S36).

label	$\delta_{\mathrm{exp},400}$	$\delta_{\mathrm{exp},1200}$	$\Delta\delta_{\mathrm{exp}}$	$\Delta\delta^{\mathrm{rel}}_{\mathrm{exp}} \times 100$
		SAP		
ax1	132.799	132.243	-0.555	-0.418
eq2	24.262	24.175	-0.088	-0.361
eq1	19.911	19.843	-0.068	-0.339
ac2	-37.332	-37.140	0.192	-0.514
ax2	-45.024	-44.789	0.235	-0.522
ac1	-81.910	-81.521	0.389	-0.475
		TSAP’		
ax1	80.642	80.384	-0.258	-0.320
eq2	14.694	14.642	-0.053	-0.360
ac1	-25.516	-25.408	0.108	-0.422
ax2	-31.636	-31.482	0.154	-0.487
ac2	-53.426	-53.214	0.211	-0.395

Table S7: Experimental shifts in ppm extracted at 298.00 K for YbDOTA(see figure S36).

label	$\delta_{\mathrm{exp},400}$	$\delta_{\mathrm{exp},1200}$	$\Delta\delta_{\mathrm{exp}}$	$\Delta\delta_{\mathrm{exp}}^{\mathrm{rel}} \times 100$
ax1-3	-504.988	-492.016	12.972	-2.569
ax1-4	-466.593	-454.473	12.120	-2.598
ax1-2	-384.988	-375.043	9.946	-2.583
ax1-1	-374.647	-365.086	9.562	-2.552
eq1-4	-234.385	-228.127	6.258	-2.670
eq2-4	-176.393	-171.571	4.822	-2.734
ax2-4	-132.710	-129.312	3.398	-2.560
eq2-3	-82.703	-80.284	2.419	-2.925
eq1-1	-62.983	-61.154	1.829	-2.904
CH_3	-51.773	-50.242	1.531	-2.958
ac2-3	211.242	206.181	-5.061	-2.396
ac1-2	216.604	212.078	-4.526	-2.090
ac1 (OH)	262.354	255.750	-6.604	-2.517
ac2-1	287.406	280.707	-6.699	-2.331
ax2-1	324.070	316.249	-7.821	-2.413
ax2-3	329.378	321.377	-8.000	-2.429
ac1-3	336.969	328.679	-8.291	-2.460
ac1-1	363.042	354.470	-8.572	-2.361

Table S8: Experimental shifts in ppm extracted at 298.00 K for DyHPDO3A in SAP conformation (see figure S37).

label	$\delta_{\text{exp},400}$	$\delta_{\text{exp},1200}$	$\Delta\delta_{\text{exp}}$	$\Delta\delta_{\text{exp}}^{\text{rel}} \times 100$
		SAP		
ac1 (OH)	-79.368	-79.000	0.369	-0.464
ac1-1	-73.329	-72.992	0.337	-0.460
ax2-1	-67.594	-67.329	0.265	-0.392
ac1-3	-66.254	-65.957	0.297	-0.449
ac1-2	-61.462	-61.204	0.259	-0.421
ax2-3	-53.372	-53.160	0.213	-0.399
ac2-1	-52.319	-52.105	0.214	-0.409
ac2-3	-40.572	-40.396	0.177	-0.436
ac2 (OH)	-27.473	-27.308	0.165	-0.599
CH	-21.615	-21.485	0.130	-0.603
ac2-2	-4.996	-4.967	0.029	-0.578
eq1-1	20.489	20.404	-0.084	-0.411
eq2-3	22.205	22.104	-0.101	-0.456
eq2-4	38.223	38.053	-0.169	-0.443
eq1-4	47.792	47.618	-0.175	-0.366
ax1-2	83.078	82.744	-0.334	-0.402
ax1-1	106.847	106.437	-0.410	-0.383
ax1-4	124.568	124.068	-0.500	-0.401
ax1-3	132.097	131.551	-0.546	-0.413
		TSAP′		
ac1-2	-35.5227	-35.3185	0.2042	-0.5748
eq2-4	91.0845	90.8421	-0.2424	-0.2661

Table S9: Experimental shifts in ppm extracted at 298.00 K for YbHPDO3A (see figure S37).

S4 QC calculations and CF/LF parameters

The list of identification codes for crystal structures from CCDC used for optimization is the following: NiSAL-HDPT, SALDNI; NiSAL-MeDPT, SAIMNI; CoTp$_2$, HPYBCO; DyDOTA TSAP and YbDOTA TSAP (from TmDOTA TSAP), LUQCEF; DyDOTA SAP and YbDOTA SAP (from DyDOTA SAP), LUQCAB; DyHPDO3A SAP and YbHPDO3A SAP (from YHPDO3A SAP), POHLAZ; DyHPDO3A TSAP and YbHPDO3A TSAP (from GdHPDO3A TSAP), POHKUS.

Below, a summary of the computational protocols applied throughout this work is presented:

1. CASSCF-(SC)NEVPT2[8, 9, 10, 11], with relativistic correction DKH, relativistically adapted basis DKH-def2-TZVP[12] and resolution of the identity (RI) approximation. The algorithm for automatically generating (AutoAux) auxiliary basis sets (ABS)[13] was used. The active spaces included only the metal orbitals, and the AILFT functionality was activated with the dedicated *actorbs* flag. The magnetic properties where computed at the QDPT level and their values from effective Hamiltonian were used.

2. CASSCF, with relativistic correction DKH and relativistically adapted basis DKH-def2-TZVP, with RI approximation and automatically generated ABS. Different orbitals were required for the metal ion (SARC2-DKH-QZVP) and H atoms (DKH-def2-SVP). Guess molecular orbitals were generated from previous *mergefrag* operation using the free ion and the ligand-only calculation results by a dedicated ORCA tool. The active spaces included only the metal orbitals, and the AILFT functionality was activated with the dedicated *actorbs* flag. The magnetic properties where computed at the QDPT level and their values from effective Hamiltonian were used.

3. Structure optimization with B3LYP functional and Grimme's dispersion correction (D3BJ)[14, 15]. The chosen basis sets were def2-SVP and def2/J[16] as ABS. The Coulomb term was treated via RI and the exchange term via seminumerical integration (RIJCOSX)[17, 18, 19]. Conductor-like polarizable continuum model with the sample's solvent (CPCM) was used.

4. Computation of NMR/EPR parameters[20, 21, 22, 23, 24] with B3LYP functional and Grimme's dispersion correction (D3BJ). The relativistic correction DKH and relativistically adapted basis DKH-def2-TZVP were used, with def2/J as ABS. The Coulomb term was treated via RI and the exchange term via seminumerical integration (RIJCOSX).

S5 Rules of thumb derivation in high temperature approximation

S5.1 The transition metal case

In the spin Hamiltonian approximation, the field-independent shielding tensor and susceptibility tensor can be written as

$$\sigma_{kl} = \langle\langle \frac{\partial H}{\partial B_0^k}\frac{\partial H}{\partial M^l}\rangle\rangle = \frac{\mu_\mathrm{B}}{\gamma}\sum_{ij}\langle\langle S_i S_j\rangle\rangle g_{ki}A_{lj}, \tag{S7}$$

$$\chi_{kl} = -\mu_0\langle\langle \frac{\partial H}{\partial B_0^k}\frac{\partial H}{\partial B_0^l}\rangle\rangle = -\mu_0\mu_\mathrm{B}^2\sum_{ij}\langle\langle S_i S_j\rangle\rangle g_{ki}g_{lj}. \tag{S8}$$

The direct field dependence tensor can be written as

$$\tau_{jkli} = \frac{1}{3!}\langle\langle \frac{\partial H}{\partial B_0^j}\frac{\partial H}{\partial B_0^k}\frac{\partial H}{\partial B_0^l}\frac{\partial H}{\partial M^i}\rangle\rangle = \frac{\mu_\mathrm{B}^3}{6\gamma}\sum_{pqrs}\langle\langle S_p S_q S_r S_s\rangle\rangle g_{jp}g_{kq}g_{lr}A_{is}. \tag{S9}$$

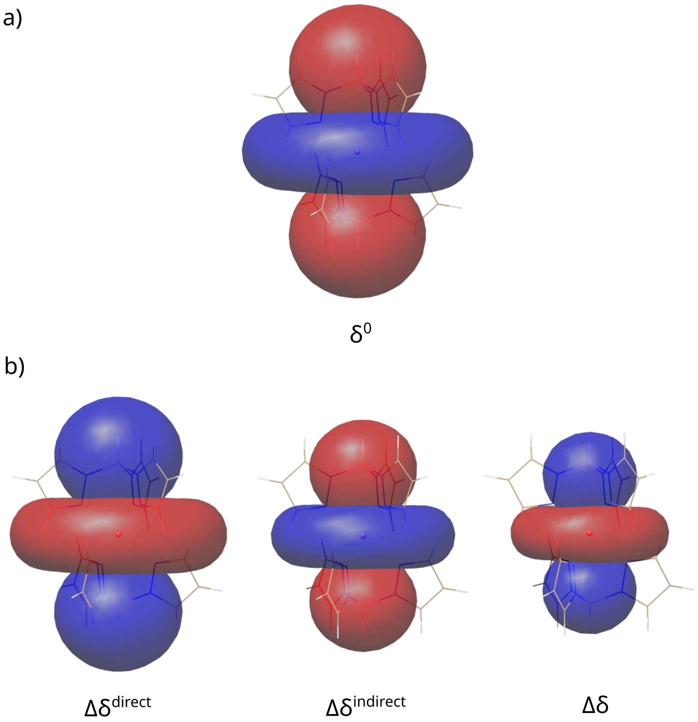

δ^0

$\Delta\delta^{\text{direct}}$ $\Delta\delta^{\text{indirect}}$ $\Delta\delta$

Figure S24: Isosurfaces (at 50 ppm (a) and 1 ppm (b)) for the CoTp_2 complex (*vide infra*), showing the field-independent (panel a) and field-dependent (panel b) PCS contributions, from left to right: $\Delta\delta^{\text{direct}}$, $\Delta\delta^{\text{indirect}}$, $\Delta\delta$. These are computed as the difference between the shifts at zero field and those computed at a 1.2 GHz ^{1}H Larmor frequency, at 298 K. Simulation parameters are obtained from a CASSCF(7,5)-NEVPT2 calculation using ORCA (see protocol (1) in S4). The direct and indirect contributions are of opposite sign, with the direct field effect being dominant.

One can show that the spin dyadic and spin tetradic can be approximated in the high-temperature limit as

$$\langle\langle S_i S_j \rangle\rangle = -\beta \delta_{ij} \frac{S(S+1)}{3} + \mathcal{O}(\beta^2), \tag{S10}$$

$$\langle\langle S_i S_j S_k S_l \rangle\rangle = \beta^3 \frac{S(S+1)(2S^2+2S+1)}{45} \left[\delta_{ij}\delta_{kl} + \delta_{ik}\delta_{jl} + \delta_{il}\delta_{jk}\right] + \mathcal{O}(\beta^4). \tag{S11}$$

In the following, we only retain the lowest-order terms in β and neglect all higher-order ones.

To derive equations 7 and 8 of the main text, we start from the point-dipole approximation and use the SH formalism, where

$$\mathbf{A} = \frac{3\mu_{\mathrm{B}}\mu_0\hbar\gamma}{4\pi R^3}(\hat{\mathbf{R}}\hat{\mathbf{R}}^{\mathrm{T}})^{\mathrm{aniso}}\mathbf{g}. \tag{S12}$$

In this framework, it is possible to demonstrate that $\Delta\delta^{\mathrm{PC,indirect}}$ is proportional to:

$$\left(\left(\frac{1}{3}\mathbf{G}^{(2:1)}\mathbf{G} - \mathbf{G}^2\right)(\hat{\mathbf{R}}\hat{\mathbf{R}}^{\mathrm{T}})^{\mathrm{aniso}}\right)^{(2:1)}, \tag{S13}$$

while $\Delta\delta^{\mathrm{PC,direct}}$ is proportional to:

$$\left(\left(\mathbf{G}^{(2:1)}\mathbf{G} + 2\mathbf{G}^2\right)(\hat{\mathbf{R}}\hat{\mathbf{R}}^{\mathrm{T}})^{\mathrm{aniso}}\right)^{(2:1)}, \tag{S14}$$

with $\mathbf{G} = \mathbf{g}\mathbf{g}^{\mathrm{T}}$ and $(\hat{\mathbf{R}}\hat{\mathbf{R}}^{\mathrm{T}})^{\mathrm{aniso}} = (\hat{\mathbf{R}}\hat{\mathbf{R}}^{\mathrm{T}}) - \frac{1}{3}(\hat{\mathbf{R}}\hat{\mathbf{R}}^{\mathrm{T}})^{(2:1)}\mathbb{I}$. This means that the isoshift surfaces of the $\delta^{\mathrm{PC},0}$, as well as $\Delta\delta^{\mathrm{PC,direct}}$ and $\Delta\delta^{\mathrm{PC,indirect}}$, depend on the eigenvectors of the $\mathbf{G}$ and $\mathbf{G}^2$ tensors. Furthermore, since $\mathbf{G}^2$ has the same eigenvectors as $\mathbf{G}$, those two tensors determining the direct and indirect contributions directionality have the same eigenvectors as $\mathbf{G}$ (*vide infra*).

Equations S13 and S14 provide an answer to the following question: is it possible to have the field-dependent part governed by either one of the two contributions or will one always prevail over the other? Proceeding within the high-temperature approximation, and assuming (i) $\mathbf{g}$ does not deviate much from $g_e\mathbb{I}$ and (ii) the isotropic part of $\mathbf{G}$ dominates over the anisotropic part, which is reasonable for TM complexes, the tensor determining the angular dependence of the indirect contribution can be written as

$$\left(\frac{1}{3}\mathbf{G}^{(2:1)}\mathbf{G} - \mathbf{G}^2\right)^{\mathrm{aniso}} = \frac{1}{3}\mathbf{G}^{(2:1)}\mathbf{G}^{\mathrm{aniso}} - (\mathbf{G}^2)^{\mathrm{aniso}} \approx -\frac{1}{3}\mathbf{G}^{(2:1)}\mathbf{G}^{\mathrm{aniso}}, \tag{S15}$$

while the angular dependence of the direct contribution can be written as

$$(\mathbf{G}^{(2:1)}\mathbf{G} + 2\mathbf{G}^2)^{\mathrm{aniso}} = \mathbf{G}^{(2:1)}\mathbf{G}^{\mathrm{aniso}} + 2(\mathbf{G}^2)^{\mathrm{aniso}} \approx \frac{7}{3}\mathbf{G}^{(2:1)}\mathbf{G}^{\mathrm{aniso}}. \tag{S16}$$

This gives (neglecting the prefactors) the 4th-order $\boldsymbol{\tau}$ tensor contracted over 2 indices. Calculating the ratio and taking into account the different prefactors, one obtains the ratio of the direct and the indirect contribution to the field-dependence of PCS

$$\frac{\Delta\delta_{\mathrm{HT}}^{\mathrm{PC,direct}}}{\Delta\delta_{\mathrm{HT}}^{\mathrm{PC,indirect}}} = -0.7\frac{2S^2+2S+1}{S(S+1)}. \tag{S17}$$

This expression gives ratios of -2.33 for $S = 1/2$, -1.75 for $S = 1$, -1.59 for $S = 3/2$ etc., and approaches an asymptotic value of -1.4 for large S. This implies that, in general, the direct and indirect contributions will have opposite signs and that the direct contribution will always be larger.

Another aspect that needs to be addressed is the difference between the PCS and the Fermi-contact shift case, where $\mathbf{A} = A_{\text{iso}}\mathbb{I}$. In the latter case, the self-orientation contribution is proportional to $\frac{1}{3}(\mathbf{g}\mathbf{g}^{\text{T}})^{(2:1)}\mathbf{g}^{(2:1)} - (\mathbf{g}\mathbf{g}^{\text{T}}\mathbf{g})^{(2:1)}$, whereas the saturation contribution is proportional to $(\mathbf{g}\mathbf{g}^{\text{T}})^{(2:1)}\mathbf{g}^{(2:1)} + 2(\mathbf{g}\mathbf{g}^{\text{T}}\mathbf{g})^{(2:1)}$. Under the same approximation for the $\mathbf{g}$ tensor anisotropy it is possible to prove that:

$$\frac{1}{3}(\mathbf{g}\mathbf{g}^{\text{T}})^{(2:1)}\mathbf{g}^{(2:1)} - (\mathbf{g}\mathbf{g}^{\text{T}}\mathbf{g})^{(2:1)} \approx 0, \tag{S18}$$

and

$$(\mathbf{g}\mathbf{g}^{\text{T}})^{(2:1)}\mathbf{g}^{(2:1)} + 2(\mathbf{g}\mathbf{g}^{\text{T}}\mathbf{g})^{(2:1)} \approx \frac{5}{9}(\mathbf{g}^{(2:1)})^3. \tag{S19}$$

This means that the self-orientation contribution is expected to be negligible compared to the saturation contribution. Hence, $\Delta\delta^{\text{FC}}$ will be dominated by the saturation contribution $\Delta\delta^{\text{FC,direct}}$ (in the aforementioned approximations).

On these grounds, we can estimate the ratio of the total field-dependent shift to the field-independent shift for the PC contribution as

$$\Delta\delta_{\text{HT}}^{\text{PC,rel}} = \Delta\delta^{\text{PC}}/\delta^{\text{PC},0} = -\beta^2\mu_{\text{B}}^2 B_0^2 \frac{4S^2+4S+7}{450}\mathbf{G}^{(2:1)} \approx -\beta^2\mu_{\text{B}}^2 B_0^2 \frac{8S^2+8S+14}{75}. \tag{S20}$$

whereas the ratio of the total Fermi contact field-dependent and field-independent shifts can be estimated to be

$$\Delta\delta_{\text{HT}}^{\text{FC,rel}} = \Delta\delta^{\text{FC}}/\delta^{\text{FC},0} = -\beta^2\mu_{\text{B}}^2 B_0^2 \frac{2S^2+2S+1}{150}\frac{5}{9}(\mathbf{g}^{(2:1)})^2 \approx -\beta^2\mu_{\text{B}}^2 B_0^2 \frac{4S^2+4S+2}{15}. \tag{S21}$$

The last approximation in both equations S20 and S21 is obtained by assuming all g-values equal to 2.

S5.2 The lanthanoid case

The indirect field dependence contribution to the chemical shift is given by

$$\Delta\delta^{\text{indirect}} = \left[\frac{1}{45}\frac{\beta}{\mu_0}\,\text{tr}(\boldsymbol{\sigma})\,\text{tr}(\boldsymbol{\chi}) - \frac{1}{15}\frac{\beta}{\mu_0}\,\text{tr}(\boldsymbol{\sigma}\boldsymbol{\chi})\right] B_0^2. \tag{S22}$$

For the lanthanoid case, we neglect the contact shift and assume that the point-dipole approximation is applicable to the pseudocontact shift,

$$\boldsymbol{\sigma} = -3\frac{1}{4\pi R^3}\boldsymbol{\chi}(\hat{\mathbf{R}}\hat{\mathbf{R}}^{\text{T}})^{\text{aniso}}. \tag{S23}$$

Inserting this leads to

$$\Delta\delta^{\text{indirect}} = -3\frac{1}{4\pi R^3}\frac{\beta B_0^2}{15\mu_0}\,\text{tr}\left[\left(\frac{1}{3}\,\text{tr}(\boldsymbol{\chi})\boldsymbol{\chi} - \boldsymbol{\chi}^2\right)(\hat{\mathbf{R}}\hat{\mathbf{R}}^{\text{T}})^{\text{aniso}}\right]. \tag{S24}$$

Expanding the susceptibility tensor in powers of $\beta = 1/k_{\text{B}}T$, one obtains

$$\left[\frac{1}{3}\,\text{tr}(\boldsymbol{\chi})\boldsymbol{\chi} - \boldsymbol{\chi}^2\right]^{\text{aniso}} = -\frac{1}{3}\,\text{tr}(\boldsymbol{\chi}_1)\boldsymbol{\chi}_2 + \mathcal{O}(\beta^4), \tag{S25}$$

where

$$\boldsymbol{\chi}_1 = \mu_0\mu_{\text{B}}^2 g_J^2 \frac{J(J+1)}{3}\beta\mathbf{I} \tag{S26}$$

is the part of the susceptibility tensor that is linear in β and

$$(\boldsymbol{\chi}_2)_{kl} = -\frac{\mu_0\mu_{\mathrm{B}}^2 g_J^2 \beta^2}{2}\frac{1}{2J+1}\,\mathrm{tr}[H^{(0)}(J_kJ_l + J_lJ_k)^{\mathrm{aniso}}] \tag{S27}$$

is the part of the susceptibility tensor that is quadratic in β. In the last equation, $H^{(0)}$ is the field-free Hamiltonian, which is commonly parametrized in terms of Stevens operators. Eq. (S27) is essentially Bleaney's theory for the susceptibility tensor. The resulting equation for the indirect field dependence is

$$\Delta\delta^{\mathrm{indirect}} = \frac{\beta^2\mu_{\mathrm{B}}^2 g_J^2 B_0^2 J(J+1)}{15}\frac{1}{4\pi R^3}\,\mathrm{tr}[\boldsymbol{\chi}_2(\hat{\mathbf{R}}\hat{\mathbf{R}}^{\mathrm{T}})^{\mathrm{aniso}}] + \mathcal{O}(\beta^5). \tag{S28}$$

The direct field dependence contribution to the shift is given by

$$\Delta\delta^{\mathrm{direct}} = -\frac{1}{5}\sum_{pq}\tau_{ppqq}B_0^2 \tag{S29}$$

with the $\boldsymbol{\tau}$ tensor in the point-dipole approximation given by

$$\tau_{lmnk} = -3\frac{1}{4\pi R^3}\sum_q \chi^{(3)}_{lmnq}(\hat{\mathbf{R}}\hat{\mathbf{R}}^{\mathrm{T}})^{\mathrm{aniso}}_{qk}. \tag{S30}$$

Inserting this equation gives

$$\Delta\delta^{\mathrm{direct}} = \frac{3B_0^2}{5}\frac{1}{4\pi R^3}\,\mathrm{tr}[\boldsymbol{\chi}^{(3),\mathrm{red}}(\hat{\mathbf{R}}\hat{\mathbf{R}}^{\mathrm{T}})^{\mathrm{aniso}}]. \tag{S31}$$

It becomes clear from this equation that the direct field dependence is determined by the anisotropy of the tensor $\boldsymbol{\chi}^{(3),\mathrm{red}}$, which is the "reduced" hypersusceptibility tensor, i.e., a Cartesian second-order tensor that is obtained by contracting the fourth-order hypersusceptibility tensor over a pair of indices,

$$\chi^{(3),\mathrm{red}}_{nq} = \sum_p \chi^{(3)}_{ppnq} = -\frac{\mu_0}{3!}\sum_p \langle\langle H_pH_pH_nH_q\rangle\rangle. \tag{S32}$$

Here, $H_p = \mu_{\mathrm{B}}g_JJ_p$ is the derivative of the effective Hamiltonian with respect to the pth component of the external magnetic field. The quantity on the right-hand side can be written as

$$\begin{aligned}\langle\langle H_kH_lH_mH_n\rangle\rangle &= S^{(klmn)}\left[\frac{\beta}{8\mu_0^2}\chi_{kl}\chi_{mn}\right] - S^{(lmn)}\frac{1}{Z}T_3^{(4)}\\ &= \frac{\beta}{\mu_0^2}\left[\chi_{kl}\chi_{mn} + \chi_{km}\chi_{ln} + \chi_{kn}\chi_{lm}\right] - S^{(lmn)}\frac{1}{Z}T_3^{(4)}\\ &= \langle\langle H_kH_lH_mH_n\rangle\rangle^{\mathrm{1st}} + \langle\langle H_kH_lH_mH_n\rangle\rangle^{\mathrm{2nd}}.\end{aligned} \tag{S33}$$

$S^{(klmn)}$ and $S^{(lmn)}$ are the symmetrization operators over the indices $klmn$ and lmn, respectively; see the appendix of our previous publication for details.[25] The 1st part leads to the contribution

$$\boldsymbol{\chi}^{(3),\mathrm{red,1st}} = -\frac{\beta}{3!\mu_0}\left[\mathrm{tr}(\boldsymbol{\chi})\boldsymbol{\chi} + 2\boldsymbol{\chi}^2\right]. \tag{S34}$$

Expanding this once more in powers of β gives

$$[\boldsymbol{\chi}^{(3),\mathrm{red,1st}}]^{\mathrm{aniso}} = -\frac{\beta}{3!\mu_0}\frac{7}{3}\,\mathrm{tr}(\boldsymbol{\chi}_1)\boldsymbol{\chi}_2 + \mathcal{O}(\beta^5). \tag{S35}$$

For the 2nd part, we first note that an expansion in powers of β gives

$$\begin{aligned}&\langle\langle H_k H_l H_m H_n \rangle\rangle^{\text{2nd}} = \\ &-\frac{1}{24(2J+1)}\left[\operatorname{tr}\left(S^{(klmn)} H_k H_l H_m H_n\right)\beta^3 - \operatorname{tr}\left(H^{(0)} S^{(klmn)} H_k H_l H_m H_n\right)\beta^4\right] + \mathcal{O}(\beta^5).\end{aligned} \tag{S36}$$

The β^3 term only contributes to the isotropic part of $\chi^{(3),\text{red,2nd}}$, such that

$$\left[\chi^{(3),\text{red,2nd}}\right]^{\text{aniso}}_{mn} = -\frac{\mu_0}{3!4!(2J+1)} \operatorname{tr}\left\{H^{(0)}\left[\sum_k \left(S^{(klmn)} H_k H_l H_m H_n\right)_{k=l}\right]^{\text{aniso}}\right\}\beta^4 + \mathcal{O}(\beta^5). \tag{S37}$$

Within the model space spanned by the $2J+1$ states of the lowest J-manifold, there is only a single linearly independent set of $k = 2$ spherical tensor operators. This means that all traceless, symmetric, order 2, Cartesian tensor operators must be proportional to each other. For the operator in the above equation, this allows us to write

$$\left[\sum_k \left(S^{(klmn)} J_k J_l J_m J_n\right)_{k=l}\right]^{\text{aniso}} = 2(6J^2+6J-5)\left[J_m J_n + J_n J_m\right]^{\text{aniso}}. \tag{S38}$$

Comparing with the Bleaney's theory equation Eq. (S27), one obtains

$$\left[\chi^{(3),\text{red,2nd}}\right]^{\text{aniso}}_{mn} = \frac{\mu_{\text{B}}^2 g_J^2}{3!4!} 4(6J^2+6J-5)\beta^2(\chi_2)_{mn} + \mathcal{O}(\beta^5). \tag{S39}$$

Combining the two parts of the reduced hypersusceptibility tensor yields

$$\left[\chi^{(3),\text{red}}\right]^{\text{aniso}} = -\frac{8J^2+8J+5}{3!}\frac{\beta^2\mu_{\text{B}}^2 g_J^2}{3!}\chi_2 + \mathcal{O}(\beta^5). \tag{S40}$$

Hence,

$$\Delta\delta^{\text{direct}} = -(8J^2+8J+5)\frac{B_0^2\beta^2\mu_{\text{B}}^2 g_J^2}{60}\frac{1}{4\pi R^3}\operatorname{tr}\left[\chi_2(\hat{\mathbf{R}}\hat{\mathbf{R}}^{\text{T}})^{\text{aniso}}\right] + \mathcal{O}(\beta^5). \tag{S41}$$

Combining indirect and direct contributions, the total field dependence is given by

$$\Delta\delta = -\frac{4J^2+4J+5}{60}\beta^2\mu_{\text{B}}^2 g_J^2 B_0^2 \frac{1}{4\pi R^3}\operatorname{tr}\left[\chi_2(\hat{\mathbf{R}}\hat{\mathbf{R}}^{\text{T}})^{\text{aniso}}\right] + \mathcal{O}(\beta^5). \tag{S42}$$

In contrast, the field-independent part of the shift is given by

$$\delta^0 = -\frac{1}{3}\operatorname{tr}(\boldsymbol{\sigma}) = \frac{1}{4\pi R^3}\operatorname{tr}\left[\chi_2(\hat{\mathbf{R}}\hat{\mathbf{R}}^{\text{T}})^{\text{aniso}}\right] + \mathcal{O}(\beta^3). \tag{S43}$$

Therefore, their ratio is given by

$$\Delta\delta^{\text{rel}}_{\text{HT}} = \Delta\delta/\delta^0 = -\mu_B^2 g_J^2 \frac{4J^2+4J+5}{60}\beta^2 B_0^2 + \mathcal{O}(\beta^3). \tag{S44}$$

This constitutes our "rule of thumb" estimate for the ratio of field-dependent to field-independent shift in lanthanoid complexes. We caution against taking this equation at face value: It is well-known that the ligand field splitting in many lanthanoid complexes is so large that Bleaney's theory stops being a good approximation and higher-order powers of $\beta = 1/k_{\text{B}}T$ become important. Still, the numbers obtained from this equation correlate well with the experimental $\Delta\delta^{\text{rel}}$ values and explains why this quantity is mostly determined by the lanthanoid ion and not much by the ligand environment.

S5.2.1 Rule application

To test the rule derived in this section we have selected two crystal field arrangements with opposite behavior in terms of stabilized J in the ground state. To do so, following Eq. S1 we must select crystal fields that produce limit-cases asphericities of the 4f electronic cloud. For a dysprosium(III) ion for example, this can be achieved by a strongly axial field (e.g.) trigonal bipyramidal (tbp) symmetry to stabilize the oblate density of the $M_J = 15/2$ state, whereas stabilization of the $M_J = 1/2$ prolate density can be achieved with a strongly equatorial field can be used to obtain a much smaller anisotropy, like that produced from a trigonal planar symmetry (tp). For ytterbium(III) the opposite holds. The crystal field parameters used in ParaMag.jl (see Methods section of the main text) were computed with NJA-CFS[26] using the code listed in S2, from point charge models in tables S11 and S10.

Listing S2: Code snippet for the computation of the crystal field parameters from point charge models with NJA-CFS[26] used with ParaMag for the simulations in table 1 in the main text.

```
import nja_csf_v0 as nja

conf_list = ['f9', 'f13']
geom_list = ["tp", "tbp"]
for conf in conf_list:
    for geom in geom_list:
        data = nja.read_data(geom+'.inp', sph_flag = False)
        data[:,-1] *= -1
        dic_Bkq = nja.calc_Bkq(data, conf, False, False)
        dic_V = nja.from_Vint_to_Bkq_2(3, dic_Bkq, reverse=True)
        Vorca = nja.rotate_dicV(dic_V, 3, rotangle_V=[0.0,0.0,0.0],
            real=True, return_orcaV = True)
        np.savetxt("V_fromNJA_"+geom+"_"+conf+".txt", Vorca, fmt='
            %.16e')
#end
```

	charge	x	y	z
Q	-1	2.0000	0.0000	0.0000
Q	-1	-1.0000	1.7321	0.0000
Q	-1	-1.0000	-1.7321	0.0000

Table S10: Point charge model for trigonal planar symmetry. The coordinates are in Å.

	charge	x	y	z
Q	-1	2.0000	0.0000	0.0000
Q	-1	-1.0000	1.7321	0.0000
Q	-1	-1.0000	-1.7321	0.0000
Q	-1	0.0000	0.0000	2.0000
Q	-1	0.0000	0.0000	-2.0000

Table S11: Point charge model for trigonal bipyramidal symmetry. The coordinates are in Å.

S6 Simulated hyperfine shifts

S6.1 Transition metal complexes

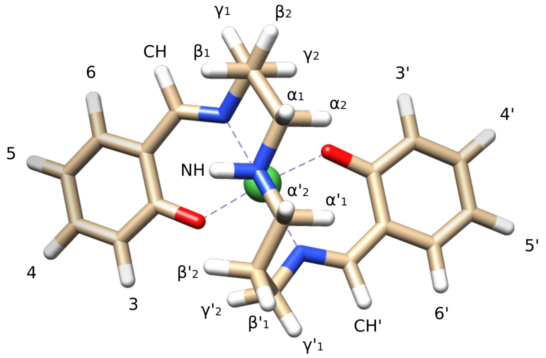

Figure S25: Protons labels for NiSAL-HDPT (and NiSAL-MeDPT)[27].

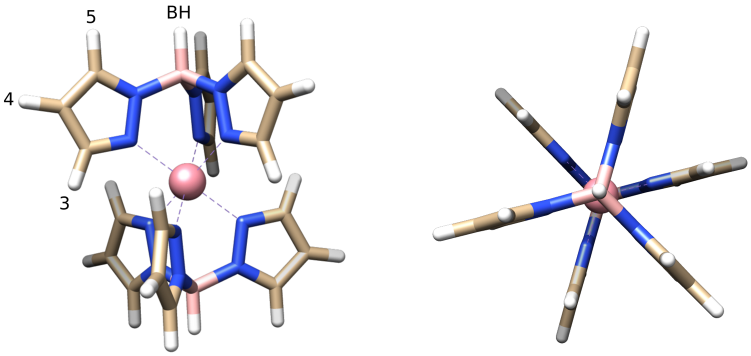

Figure S26: Proton labels of CoTp$_2$[28].

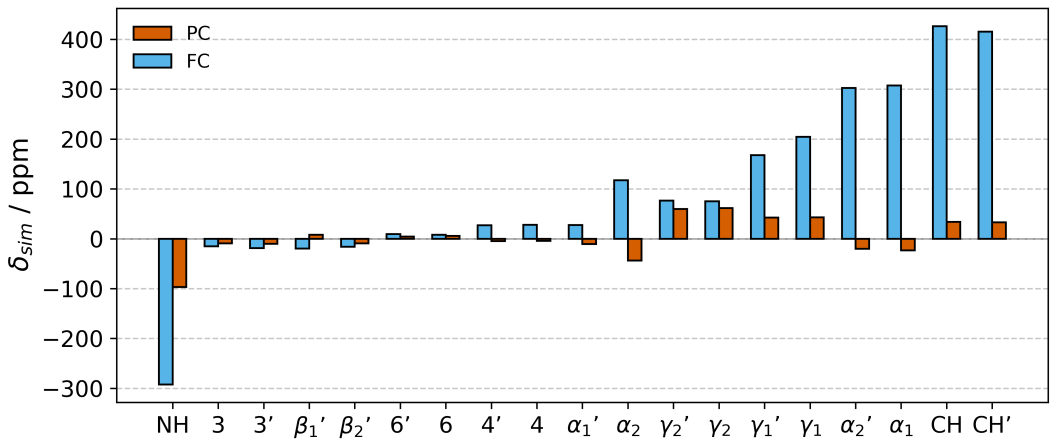

Figure S27: Barplot of simulated field-independent pseudocontact (PCS) and Fermi contact (FCS) contributions to the hyperfine shifts (in ppm) at 298.00 K for NiSAL-HDPT. PCS values were derived from AILFT parameters obtained at the CASSCF(8,5)+NEVPT2 level, while FCS values were computed using $\boldsymbol{D}$ from the same calculation combined with $\boldsymbol{g}$ and A^{iso} tensors from DFT. Atom labeling is shown in Figure S25.

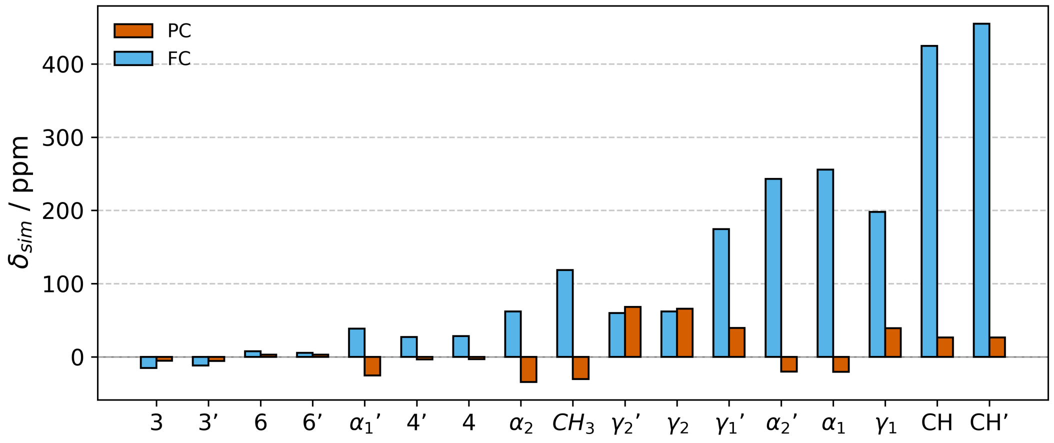

Figure S28: Barplot of simulated field-independent pseudocontact (PCS) and Fermi contact (FCS) contributions to the hyperfine shifts (in ppm) at 298.00 K for NiSAL-MeDPT. PCS values were derived from AILFT parameters obtained at the CASSCF(8,5)+NEVPT2 level, while FCS values were computed using $\boldsymbol{D}$ from the same calculation combined with $\boldsymbol{g}$ and A^{iso} tensors from DFT. Atom labeling is shown in Figure S25.

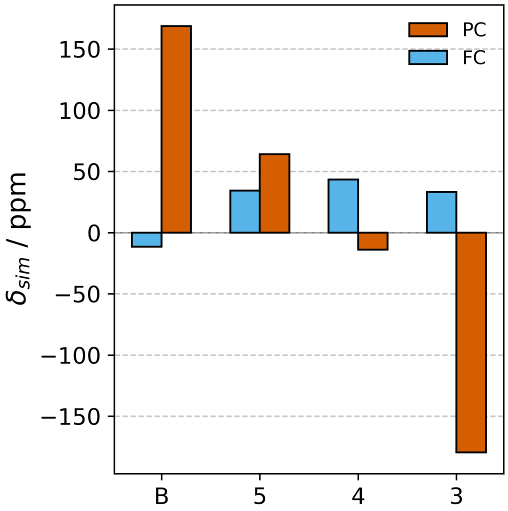

Figure S29: Barplot of simulated field-independent pseudocontact (PCS) and Fermi contact (FCS) contributions to the hyperfine shifts (in ppm) at 298.00 K for $CoTp_2$. PCS values were derived from AILFT parameters obtained at the CASSCF(7,5)+NEVPT2 level, while FCS values were computed using $\boldsymbol{D}$ from the same calculation combined with $\boldsymbol{g}$ and A^{iso} tensors from DFT. Atom labeling is shown in Figure S26.

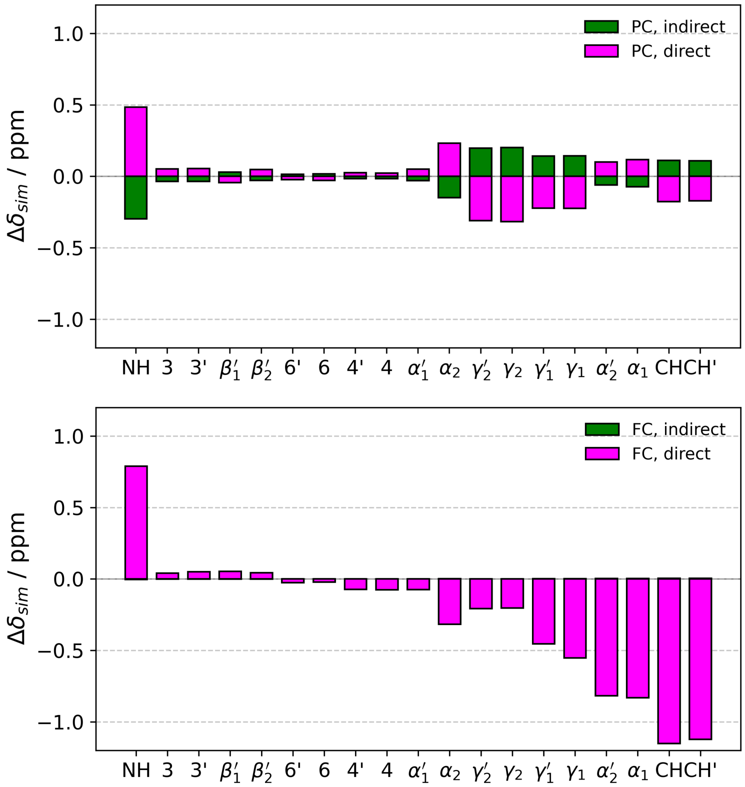

Figure S30: Barplot for direct and indirect contributions to the hyperfine shifts (pseudocontact shift, above, and Fermi contact shift, below), computed for NiSAL-HDPT complex.

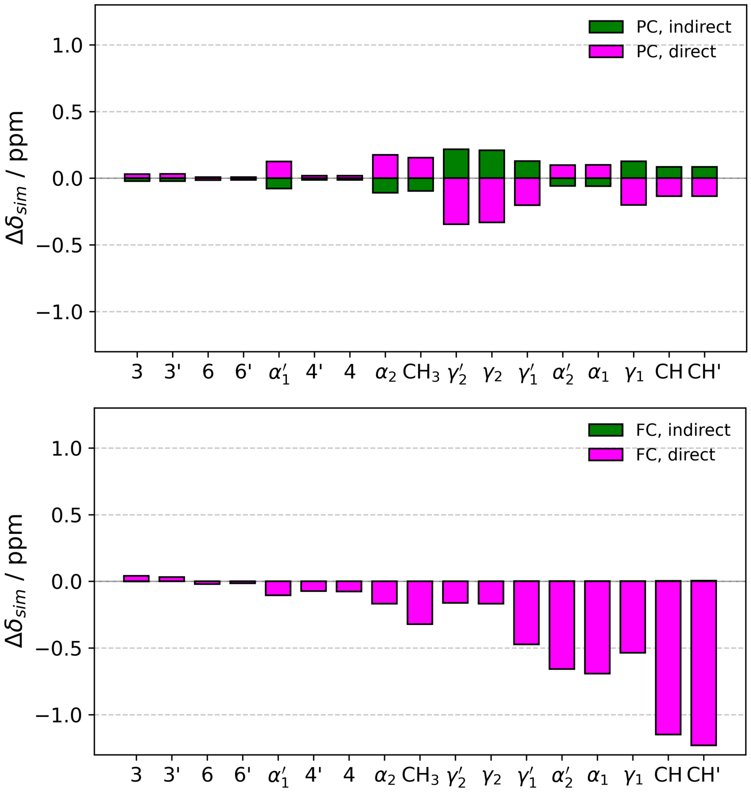

Figure S31: Barplot for direct and indirect contributions to the hyperfine shifts (pseudo-contact shift, above, and Fermi contact shift, below), computed for NiSAL-MeDPT complex.

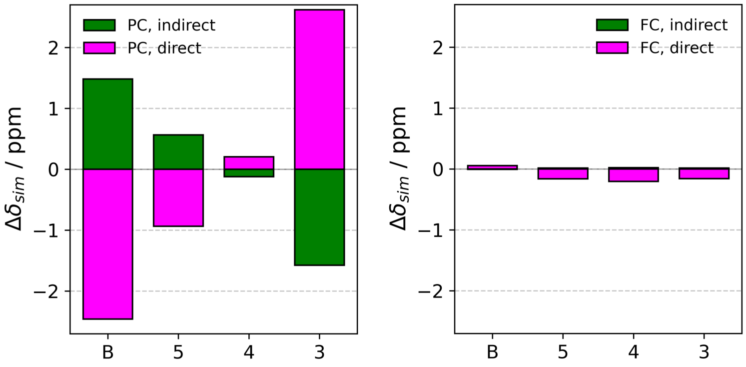

Figure S32: Barplot for direct and indirect contributions to the hyperfine shifts (pseudo-contact shift, left, and Fermi contact shift, right), computed for $CoTp_2$ complex.

label	$\delta_{\mathrm{sim},400}$	$\delta_{\mathrm{sim},1200}$	$\Delta\delta_{\mathrm{sim}}$	$\Delta\delta^{\mathrm{rel}}_{\mathrm{sim}} \times 100$
NH	-388.831	-387.858	0.973	-0.250
3	-24.481	-24.423	0.058	-0.237
3′	-28.789	-28.719	0.069	-0.241
$\beta_1{}'$	-11.780	-11.741	0.039	-0.328
$\beta_2{}'$	-25.320	-25.258	0.062	-0.244
6′	13.887	13.853	-0.034	-0.245
6	13.480	13.448	-0.032	-0.239
4′	22.447	22.382	-0.064	-0.286
4	23.799	23.731	-0.068	-0.284
$\alpha_1{}'$	16.788	16.735	-0.053	-0.317
α_2	73.823	73.589	-0.234	-0.317
$\gamma_2{}'$	136.334	136.015	-0.319	-0.234
γ_2	136.893	136.574	-0.319	-0.233
$\gamma_1{}'$	210.296	209.764	-0.532	-0.253
γ_1	247.272	246.641	-0.631	-0.255
$\alpha_2{}'$	282.252	281.477	-0.775	-0.275
α_1	284.349	283.566	-0.783	-0.275
CH	460.063	458.851	-1.212	-0.263
CH′	448.222	447.041	-1.181	-0.263

Table S12: Simulated field-dependent hyperfine shifts (ppm) at 298.00 K for NiSAL-HDPT. The shifts are obtained as the sum of pseudocontact (PCS) and Fermi contact (FCS) contributions. PCS values were derived from AILFT parameters obtained at the CASSCF(8,5)+NEVPT2 level, while FCS values were computed using $\boldsymbol{D}$ from the same calculation combined with $\boldsymbol{g}$ and A^{iso} tensors from DFT. Atom labeling is shown in Figure S25.

label	$\delta_{\text{sim},400}$	$\delta_{\text{sim},1200}$	$\Delta\delta_{\text{sim}}$	$\Delta\delta_{\text{sim}}^{\text{rel}} \times 100$
3	-20.456	-20.405	0.050	-0.247
3′	-17.695	-17.652	0.043	-0.241
6	10.650	10.624	-0.027	-0.251
6′	8.076	8.056	-0.020	-0.246
$\alpha_1{}'$	13.162	13.106	-0.056	-0.426
4′	23.630	23.564	-0.067	-0.282
4	25.013	24.943	-0.070	-0.281
α_2	27.576	27.474	-0.101	-0.367
CH_3	10.254	10.226	-0.028	-0.278
$\gamma_2{}'$	128.098	127.809	-0.289	-0.225
γ_2	127.674	127.384	-0.290	-0.227
$\gamma_1{}'$	214.051	213.506	-0.544	-0.254
$\alpha_2{}'$	222.765	222.150	-0.615	-0.276
α_1	235.054	234.405	-0.649	-0.276
γ_1	237.072	236.465	-0.607	-0.256
CH	451.150	449.956	-1.194	-0.265
CH′	481.515	480.239	-1.276	-0.265

Table S13: Simulated field-dependent hyperfine shifts (ppm) at 298.00 K for NiSAL-MeDPT. The shifts are obtained as the sum of pseudocontact (PCS) and Fermi contact (FCS) contributions. PCS values were derived from AILFT parameters obtained at the CASSCF(8,5)+NEVPT2 level, while FCS values were computed using $\boldsymbol{D}$ from the same calculation combined with $\boldsymbol{g}$ and A^{iso} tensors from DFT. Atom labeling is shown in Figure S25.

label	$\delta_{\text{sim},400}$	$\delta_{\text{sim},1200}$	$\Delta\delta_{\text{sim}}$	$\Delta\delta_{\text{sim}}^{\text{rel}} \times 100$
B	157.180	156.249	-0.931	-0.592
5	98.504	97.984	-0.520	-0.528
4	29.428	29.324	-0.105	-0.356
3	-146.144	-145.244	0.900	-0.616

Table S14: Simulated field-dependent hyperfine shifts (ppm) at 298.00 K for $CoTp_2$. The shifts are obtained as the sum of pseudocontact (PCS) and Fermi contact (FCS) contributions. PCS values were derived from AILFT parameters obtained at the CASSCF(7,5)+NEVPT2 level, while FCS values were computed using $\boldsymbol{D}$ from the same calculation combined with $\boldsymbol{g}$ and A^{iso} tensors from DFT. Atom labeling is shown in Figure S26.

label	$\delta_{\text{sim},400}$	$\delta_{\text{sim},1200}$	$\Delta\delta_{\text{sim}}$	$\Delta\delta_{\text{sim}}^{\text{rel}} \times 100$
B	125.804	123.838	-1.965	-1.562
5	89.662	88.678	-0.984	-1.107
4	29.616	29.607	-0.009	-0.029
3	-108.264	-106.342	1.922	-1.778

Table S15: Simulated field-dependent hyperfine shifts (ppm) at 298.00 K for CoTp_2. The shifts are obtained as the sum of pseudocontact (PCS) and Fermi contact (FCS) contributions. Both PCSs and FCSs were computed in the SH framework, with $\boldsymbol{g}$ and $\boldsymbol{D}$ tensors obtained at the CASSCF(7,5)+NEVPT2 level, with A tensors from DFT calculation. Atom labeling is shown in Figure S26.

label	$\delta_{\text{sim},400}$	$\delta_{\text{sim},1200}$	$\Delta\delta_{\text{sim}}$	$\Delta\delta_{\text{sim}}^{\text{rel}} \times 100$
B	128.322	127.349	-0.973	-0.758
5	89.544	88.994	-0.550	-0.618
4	31.915	31.813	-0.101	-0.317
3	-117.094	-116.142	0.952	-0.814

Table S16: Simulated field-dependent hyperfine shifts (ppm) at 298.00 K for CoTp_2. The shifts are obtained as the sum of pseudocontact (PCS) and Fermi contact (FCS) contributions. Both PCSs and FCSs were computed in the SH framework, with $\boldsymbol{A}$ and $\boldsymbol{D}$ tensors obtained at the CASSCF(7,5)+NEVPT2 level, while A^{iso} and $\boldsymbol{g}$ matrix from DFT calculation. Atom labeling is shown in Figure S26.

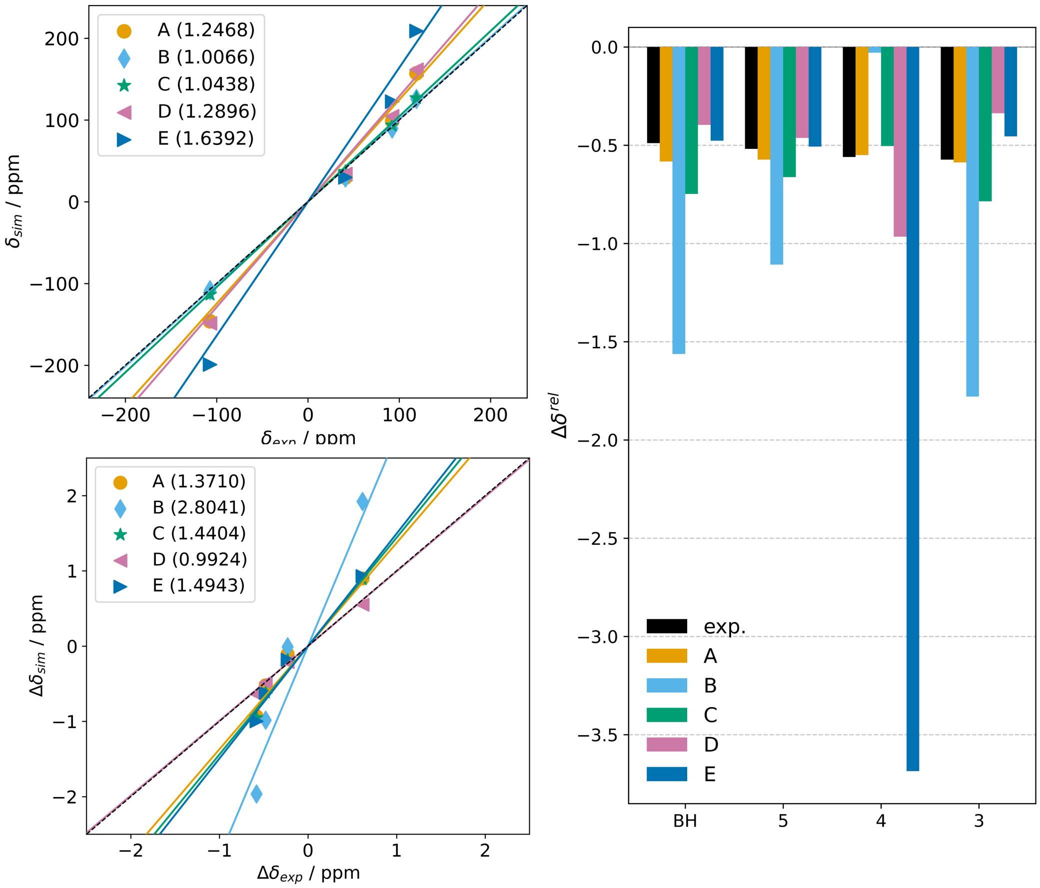

Figure S33: Comparison of performance of the different protocols tested for $\mathrm{CoTp_2}$ case. This analysis includes two scatter plots for $\Delta\delta_{\mathrm{sim}}$ and δ_{sim} against the experimental counterpart, and a bar plot of the $\Delta\delta^{\mathrm{rel}}$.
A: PCSs from AILFT (from protocol (1)) and FCSs in SH framework with $\boldsymbol{g}$ and A^{iso} from DFT (through protocol (4)) and $\boldsymbol{D}$ from ab initio (through protocol (1)).
B: PCSs and FCSs in SH framework with $\boldsymbol{A}$ from DFT (through protocol (4)) and $\boldsymbol{g}$ and $\boldsymbol{D}$ from ab initio (through protocol (1)).
C: PCSs and FCSs in SH framework with $\boldsymbol{g}$, $\boldsymbol{A}$ and $\boldsymbol{D}$ from ab initio (through protocol (1)).
D: FCSs in SH framework with A^{iso} from DFT (through protocol (4)) and $\boldsymbol{g}$ and $\boldsymbol{D}$ from ab initio (through protocol (1)) and PCSs in the ${}^4\mathrm{T}_{1g}$ adapted Hamiltonian with Δ =466 cm^{-1}, λ =147.3 cm^{-1} and σ =1.169.
E: FCSs in SH framework with A^{iso} from DFT (through protocol (4)) and $\boldsymbol{g}$ and $\boldsymbol{D}$ from ab initio (through protocol (1)) and PCSs in the ${}^4\mathrm{T}_{1g}$ adapted Hamiltonian with Δ =632 cm^{-1}, λ =147.3 cm^{-1} and σ =1.35.

S6.2 Lanthanoid complexes

Basis set reduction

In order to simulate the field-dependent δ for lanthanoid complexes, we consider solely the pseudocontact contribution, computed within the LF framework. In the case of dysprosium complexes, an additional step is required, since in this case the CASSCF calculation involves only a subset of the complete set of roots and multiplicities, i.e. 21 sextets. Therefore, before computing the second- and fourth-order susceptibilities used in the evaluation of δ^{PC}, the basis set was reduced to the lowest ${}^6H_{15/2}$ manifold.

The eigenvectors of the spin-squared operator S^2 are used to rotate the non-relativistic Hamiltonian (i.e., the one built solely from the interelectronic interaction and the crystal-field term). The rotated Hamiltonian is then diagonalized, and the eigenvectors corresponding to the correct multiplicity, identified on the basis of the S^2 eigenvalues, are selected. These eigenvectors (collected in a matrix **C**) are finally used to rotate the full Hamiltonian as $\mathbf{C}^\dagger\mathbf{HC}$, where † indicates the matrix transpose.

Double-average method

As briefly described in the main text, in the simulation protocol for the proton LnDOTA shifts, in order to reproduce the axial character of the system, the LF matrix V from the AILFT analysis was rotated in the 4 equivalent positions through 90° rotation steps around the Ln-O_w axis. The procedure was applied using the NJA-CSF software[26], and this tensor was then used in the ParaMag.jl program for the computation of the field-dependent hyperfine shifts (see listing S3).

Listing S3: Code listing for LF parameters rotation through application of the dedicated NJA-CFS routine. The function returns the AILFT ORCA matrix rotated by R Euler angles.

```
import nja_csf_v0 as nja

def test_LF_rotation_euler(conf, filename, R):

    # R = Euler angles in ZYZ scipy convention
    # the same routine can be applied using quaternions instead of
       Euler angles

    # reading AILFT from ORCA output file
    dic = nja.read_AILFT_orca6(filename, conf)
    dic_Bkq = dic['dic_bkq']
    # rotation
    dic_V = nja.from_Vint_to_Bkq_2(3, dic_Bkq, reverse=True)
    Vorca = nja.rotate_dicV(dic_V, 3, rotangle_V=R, real=True,
       return_orcaV = True)

return Vorca
#end
```

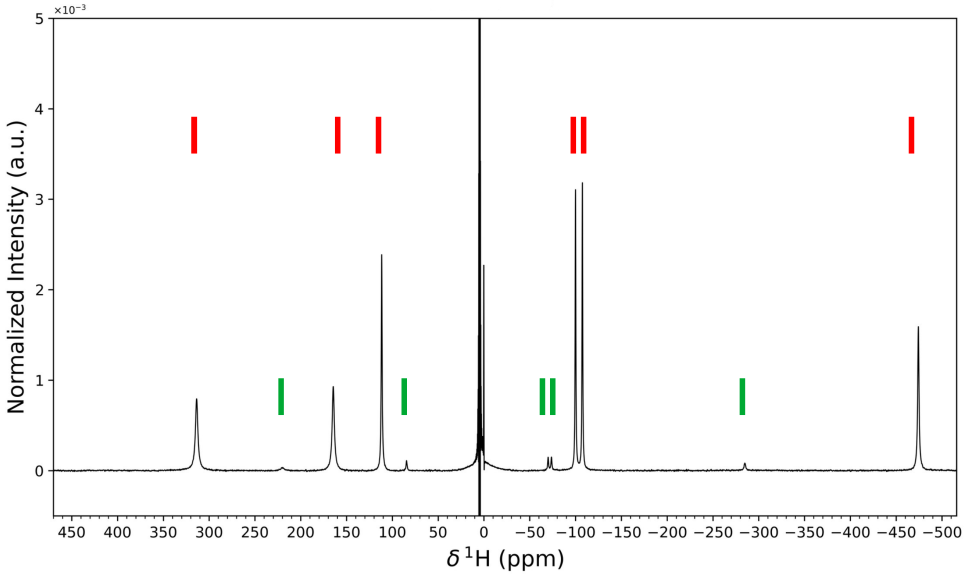

Figure S34: Experimental spectrum acquired at 400 MHz ^{1}H Larmor frequency 298.00 K of DyDOTA. The red symbols indicate protons of the SAP conformer, while the green symbols indicate protons of the TSAP conformer[29].

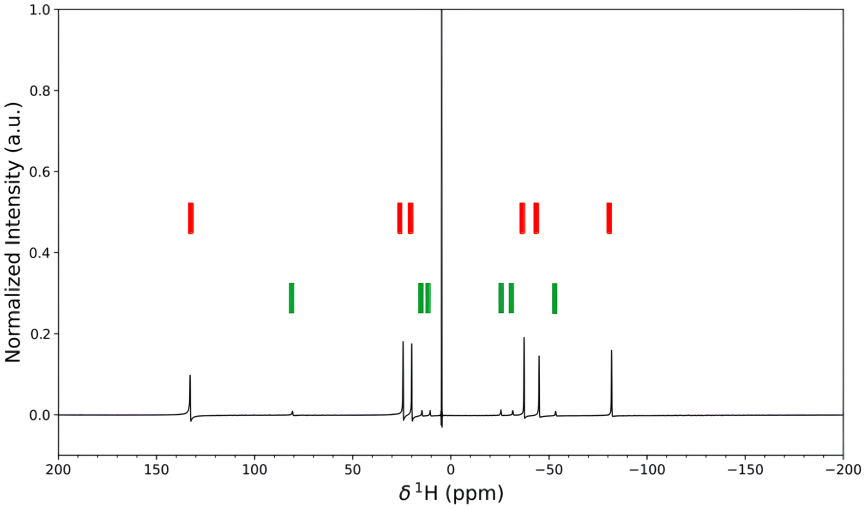

Figure S35: Experimental spectrum acquired at 400 MHz ^{1}H Larmor frequency 298.00 K of YbDOTA. The red symbols indicate protons of the SAP conformer, while the green symbols indicate protons of the TSAP' conformed[29].

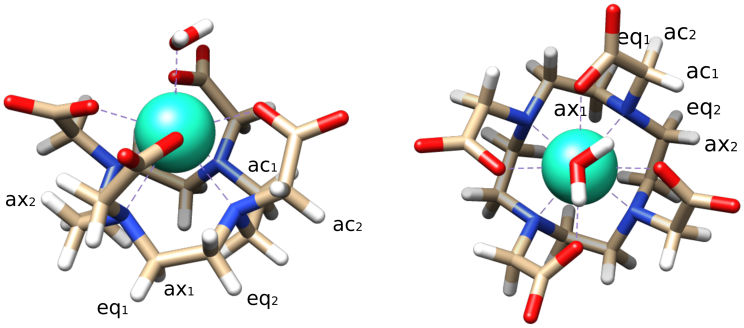

Figure S36: Proton labels of $[LnDOTA(H_2O)]^-$[29].

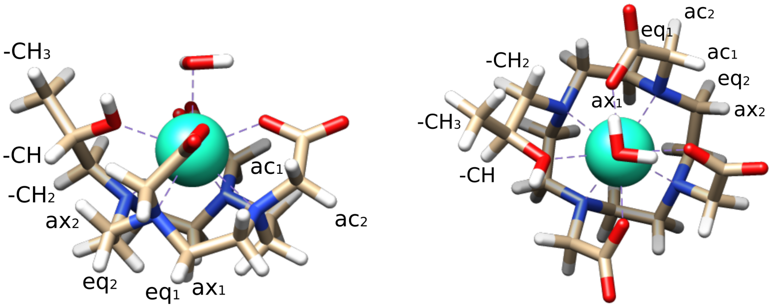

Figure S37: Proton labels of $LnHPDO3A(H_2O)$[7].

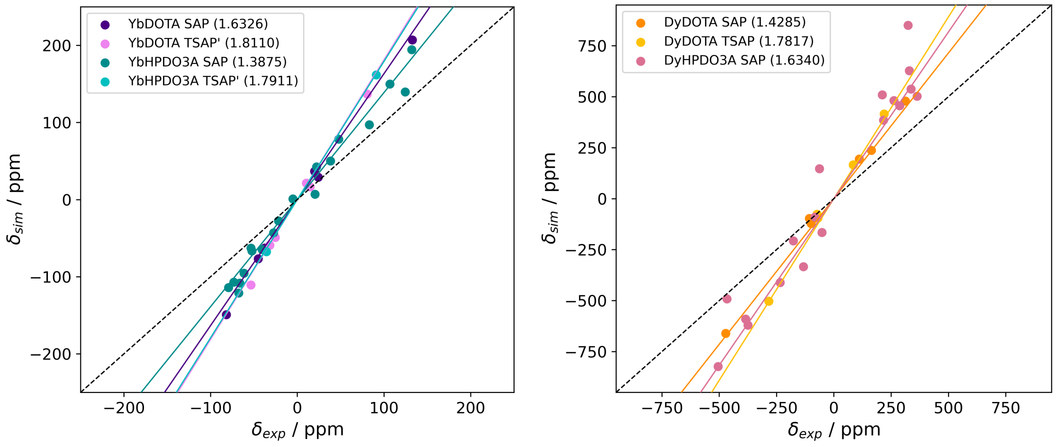

Figure S38: Comparison of simulated field-dependent hyperfine shifts computed at 400 MHz ^{1}H Larmor frequency with the experimental counterpart, for lanthanoid model complexes.

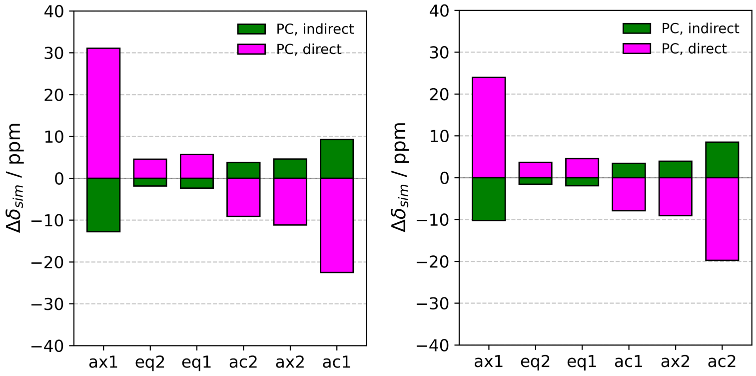

Figure S39: Barplot for direct and indirect contributions to the hyperfine shifts, computed for DyDOTA complex (SAP conformer left and TSAP right).

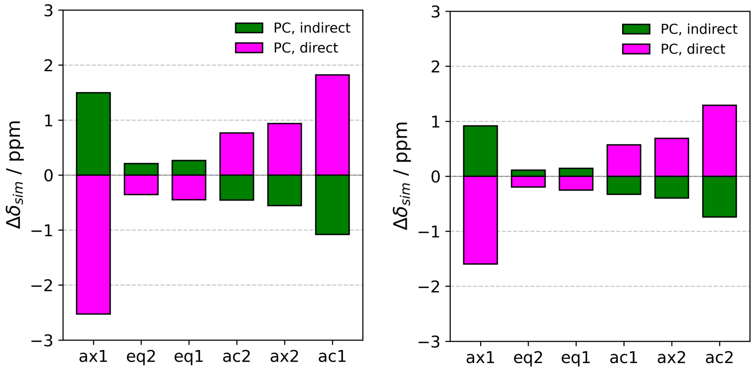

Figure S40: Barplot for direct and indirect contributions to the hyperfine shifts, computed for YbDOTA complex (SAP conformer left and TSAP' right).

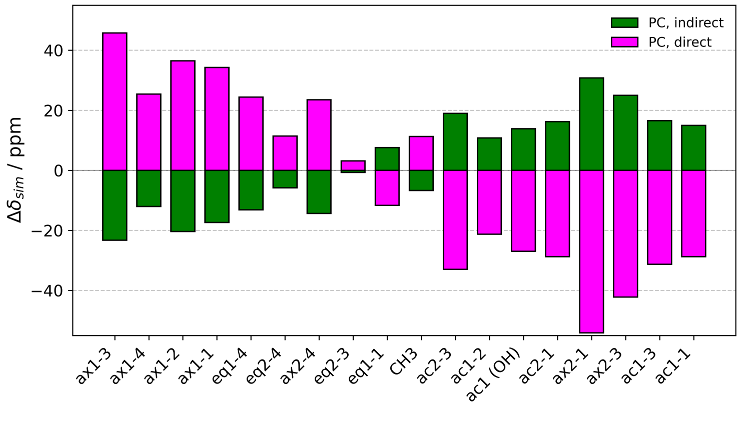

Figure S41: Barplot for direct and indirect contributions to the hyperfine shifts, computed for DyHPDO3A complex SAP conformer.

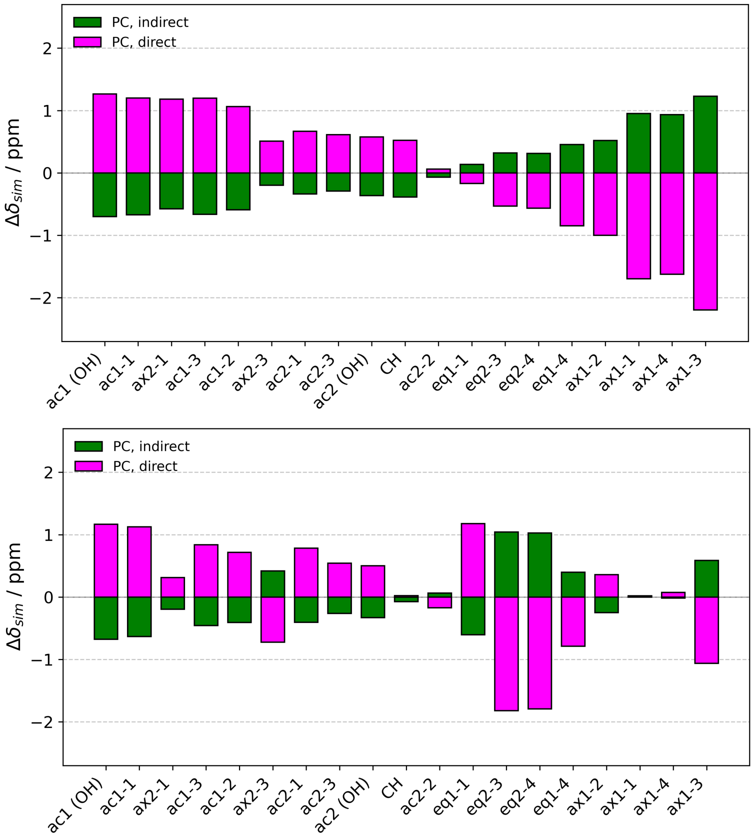

Figure S42: Barplot for direct and indirect contributions to the hyperfine shifts, computed for YbHPDO3A complex (SAP conformer above and TSAP′ below).

label	$\delta_{\mathrm{sim},400}$	$\delta_{\mathrm{sim},1200}$	$\Delta\delta_{\mathrm{sim}}$	$\Delta\delta^{\mathrm{rel}}_{\mathrm{sim}} \times 100$
SAP				
ax1	-660.375	-642.333	18.042	-2.732
eq2	-96.738	-94.095	2.643	-2.732
eq1	-121.287	-117.973	3.314	-2.732
ac2	194.105	188.802	-5.303	-2.732
ax2	236.921	230.448	-6.473	-2.732
ac1	478.619	465.543	-13.076	-2.732
TSAP				
ax1	-503.210	-489.405	13.804	-2.743
eq2	-76.499	-74.401	2.099	-2.743
eq1	-95.182	-92.571	2.611	-2.743

Table S17: Simulated field-dependent hyperfine shifts (ppm) at 298.00 K for DyDOTA. The shifts correspond solely to the pseudocontact (PCS) contribution, derived from AILFT parameters obtained at the CASSCF(9,7) level. Atom labeling is shown in Figure S36.

label	$\delta_{\text{sim},400}$	$\delta_{\text{sim},1200}$	$\Delta\delta_{\text{sim}}$	$\Delta\delta_{\text{sim}}^{\text{rel}} \times 100$
SAP				
ax1	-670.710	-652.391	18.318	-2.731
eq2	-98.225	-95.542	2.683	-2.719
eq1	-123.147	-119.784	3.363	-2.725
ac2	197.161	191.777	-5.385	-2.730
ax2	240.595	234.024	-6.571	-2.729
ac1	486.046	472.772	-13.275	-2.731
TSAP				
ax1	-498.731	-485.048	13.683	-2.744
eq2	-75.861	-73.780	2.081	-2.761
eq1	-94.393	-91.803	2.590	-2.745

Table S18: Simulated single-averaged field-dependent hyperfine shifts (ppm) at 298.00 K for DyDOTA. The shifts correspond solely to the pseudocontact (PCS) contribution, derived from AILFT parameters obtained at the CASSCF(9,7) level. Atom labeling is shown in Figure S36.

label	$\delta_{\text{sim},400}$	$\delta_{\text{sim},1200}$	$\Delta\delta_{\text{sim}}$	$\Delta\delta_{\text{sim}}^{\text{rel}} \times 100$
SAP				
ax1	206.964	205.952	-1.012	-0.489
eq2	29.032	28.890	-0.142	-0.489
eq1	36.673	36.494	-0.179	-0.489
ac2	-62.747	-62.440	0.307	-0.489
ax2	-76.682	-76.307	0.375	-0.489
ac1	-149.241	-148.511	0.730	-0.489
TSAP'				
ax1	136.732	136.087	-0.645	-0.472
eq2	16.632	16.554	-0.078	-0.472
eq1	21.417	21.316	-0.101	-0.472
ac1	-48.978	-48.746	0.231	-0.472
ax2	-59.060	-58.781	0.279	-0.472
ac2	-110.706	-110.184	0.522	-0.472

Table S19: Simulated field-dependent hyperfine shifts (ppm) at 298.00 K for YbDOTA. The shifts correspond solely to the pseudocontact (PCS) contribution, derived from AILFT parameters obtained at the CASSCF(13,7) level. Atom labeling is shown in Figure S36.

label	$\delta_{\mathrm{sim},400}$	$\delta_{\mathrm{sim},1200}$	$\Delta\delta_{\mathrm{sim}}$	$\Delta\delta^{\mathrm{rel}}_{\mathrm{sim}} \times 100$
		SAP		
ax1	210.456	209.427	-1.028	-0.489
eq2	29.502	29.358	-0.144	-0.484
eq1	37.271	37.089	-0.182	-0.487
ac2	-63.803	-63.491	0.312	-0.489
ax2	-77.994	-77.613	0.381	-0.488
ac1	-151.727	-150.985	0.741	-0.489
		TSAP′		
ax1	143.830	143.152	-0.678	-0.472
eq2	17.496	17.414	-0.083	-0.471
eq1	22.532	22.426	-0.106	-0.471
ac1	-51.516	-51.273	0.243	-0.472
ax2	-62.124	-61.831	0.293	-0.472
ac2	-116.433	-115.884	0.549	-0.472

Table S20: Simulated single-averaged field-dependent hyperfine shifts (ppm) at 298.00 K for YbDOTA. The shifts correspond solely to the pseudocontact (PCS) contribution, derived from AILFT parameters obtained at the CASSCF(13,7) level. Atom labeling is shown in Figure S36.

label	$\delta_{\text{sim},400}$	$\delta_{\text{sim},1200}$	$\Delta\delta_{\text{sim}}$	$\Delta\delta_{\text{sim}}^{\text{rel}} \times 100$
ax1-3	-823.383	-800.872	22.511	-2.734
ax1-4	-491.257	-477.873	13.384	-2.725
ax1-2	-590.607	-574.449	16.158	-2.736
ax1-1	-620.122	-603.182	16.940	-2.732
eq1-4	-411.203	-399.932	11.271	-2.741
eq2-4	-206.965	-201.316	5.649	-2.729
ax2-4	-333.349	-324.191	9.157	-2.747
eq2-3	-90.114	-87.649	2.465	-2.735
eq1-1	147.263	143.187	-4.075	-2.767
CH_3	-165.388	-160.829	4.559	-2.757
ac2-3	509.357	495.371	-13.986	-2.746
ac1-2	384.682	374.222	-10.460	-2.719
ac1 (OH)	480.613	467.528	-13.085	-2.723
ac2-1	456.022	443.511	-12.511	-2.743
ax2-1	850.103	826.805	-23.299	-2.741
ax2-3	627.149	609.968	-17.181	-2.740
ac1-3	537.396	522.660	-14.736	-2.742
ac1-1	502.187	488.422	-13.766	-2.741

Table S21: Simulated field-dependent hyperfine shifts (ppm) at 298.00 K for DyHPDO3A in SAP conformation. The shifts correspond solely to the pseudocontact (PCS) contribution, derived from AILFT parameters obtained at the CASSCF(9,7) level. Atom labeling is shown in Figure S37.

label	$\delta_{\text{sim},400}$	$\delta_{\text{sim},1200}$	$\Delta\delta_{\text{sim}}$	$\Delta\delta^{\text{rel}}_{\text{sim}} \times 100$
		SAP		
ac1 (OH)	-114.124	-113.556	0.568	-0.498
ac1-1	-107.025	-106.495	0.530	-0.495
ax2-1	-121.134	-120.527	0.607	-0.501
ac1-3	-108.333	-107.797	0.536	-0.495
ac1-2	-95.334	-94.860	0.474	-0.497
ax2-3	-62.882	-62.569	0.313	-0.498
ac2-1	-66.496	-66.166	0.330	-0.497
ac2-3	-64.669	-64.347	0.322	-0.498
ac2 (OH)	-43.078	-42.864	0.214	-0.498
CH	-27.616	-27.482	0.134	-0.485
ac2-2	0.968	0.961	-0.007	-0.723
eq1-1	6.874	6.842	-0.032	-0.466
eq2-3	42.468	42.256	-0.212	-0.499
eq2-4	50.061	49.811	-0.250	-0.499
eq1-4	78.340	77.948	-0.392	-0.500
ax1-2	97.111	96.631	-0.480	-0.494
ax1-1	149.887	149.143	-0.744	-0.497
ax1-4	139.549	138.858	-0.690	-0.495
ax1-3	194.462	193.495	-0.968	-0.498
		TSAP’		
ac1-2	-67.512	-67.203	0.309	-0.458
eq2-4	161.630	160.865	-0.766	-0.474

Table S22: Simulated field-dependent hyperfine shifts (ppm) at 298.00 K for YbHPDO3A. The shifts correspond solely to the pseudocontact (PCS) contribution, derived from AILFT parameters obtained at the CASSCF(13,7) level. Atom labeling is shown in Figure S37.

References

[1] Giacomo Parigi, Enrico Ravera, and Claudio Luchinat. “Magnetic susceptibility and paramagnetism-based NMR”. In: *Progress in Nuclear Magnetic Resonance Spectroscopy* 114 (2019), pp. 211–236.

[2] Francesca Camponeschi et al. “Paramagnetic 1H NMR spectroscopy to investigate the catalytic mechanism of radical S-adenosylmethionine enzymes”. In: *Journal of molecular biology* 431.22 (2019), pp. 4514–4522.

[3] Lucia Banci et al. “Biomolecular NMR at 1.2 GHz”. In: *arXiv preprint arXiv:1910.07462* (2019).

[4] Niels Karschin et al. "Extension and improvement of the methanol-d4 NMR thermometer calibration". In: *Magnetic Resonance in Chemistry* 60.2 (2022), pp. 203–209.

[5] Letizia Fiorucci et al. "Extracting Trends From NMR Data With TrAGICo: A Python Toolbox". In: *Magnetic Resonance in Chemistry* (2025).

[6] Letizia Fiorucci et al. "Applications of Fast Iterative Filtering in NMR Spectroscopy: Baseline Correction". In: *Magnetic Resonance in Chemistry* (2025).

[7] Daniela Delli Castelli et al. "Combined high resolution NMR and 1H and 17O relaxometric study sheds light on the solution structure and dynamics of the lanthanide (III) complexes of HPDO3A". In: *Inorganic chemistry* 52.12 (2013), pp. 7130–7138.

[8] Christian Kollmar et al. "A perturbation-based super-CI approach for the orbital optimization of a CASSCF wave function". In: *Journal of computational chemistry* 40.14 (2019), pp. 1463–1470.

[9] Christian Kollmar et al. "An efficient implementation of the NEVPT2 and CASPT2 methods avoiding higher-order density matrices". In: *The Journal of Chemical Physics* 155.23 (2021).

[10] Yang Guo, Kantharuban Sivalingam, and Frank Neese. "Approximations of density matrices in N-electron valence state second-order perturbation theory (NEVPT2). I. Revisiting the NEVPT2 construction". In: *The Journal of Chemical Physics* 154.21 (2021).

[11] Frank Neese. "The SHARK integral generation and digestion system". In: *Journal of Computational Chemistry* 44.3 (2023), pp. 381–396.

[12] Florian Weigend and Reinhart Ahlrichs. "Balanced basis sets of split valence, triple zeta valence and quadruple zeta valence quality for H to Rn: Design and assessment of accuracy". In: *Physical Chemistry Chemical Physics* 7.18 (2005), pp. 3297–3305.

[13] Georgi L Stoychev, Alexander A Auer, and Frank Neese. "Automatic generation of auxiliary basis sets". In: *Journal of chemical theory and computation* 13.2 (2017), pp. 554–562.

[14] Stefan Grimme et al. "A consistent and accurate ab initio parametrization of density functional dispersion correction (DFT-D) for the 94 elements H-Pu". In: *The Journal of chemical physics* 132.15 (2010).

[15] Stefan Grimme, Stephan Ehrlich, and Lars Goerigk. "Effect of the damping function in dispersion corrected density functional theory". In: *Journal of computational chemistry* 32.7 (2011), pp. 1456–1465.

[16] Florian Weigend. "Accurate Coulomb-fitting basis sets for H to Rn". In: *Physical chemistry chemical physics* 8.9 (2006), pp. 1057–1065.

[17] Frank Neese. "An improvement of the resolution of the identity approximation for the formation of the Coulomb matrix". In: *Journal of computational chemistry* 24.14 (2003), pp. 1740–1747.

[18] Frank Neese et al. "Efficient, approximate and parallel Hartree–Fock and hybrid DFT calculations. A 'chain-of-spheres' algorithm for the Hartree–Fock exchange". In: *Chemical Physics* 356.1-3 (2009), pp. 98–109.

[19] Benjamin Helmich-Paris et al. "An improved chain of spheres for exchange algorithm". In: *The Journal of Chemical Physics* 155.10 (2021).

[20] Frank Neese. "Metal and ligand hyperfine couplings in transition metal complexes: The effect of spin–orbit coupling as studied by coupled perturbed Kohn–Sham theory". In: *The Journal of chemical physics* 118.9 (2003), pp. 3939–3948.

[21] Frank Neese. "Efficient and accurate approximations to the molecular spin-orbit coupling operator and their use in molecular g-tensor calculations". In: *The Journal of chemical physics* 122.3 (2005).

[22] Sebastian Sinnecker and Frank Neese. “Spin- Spin Contributions to the Zero-Field Splitting Tensor in Organic Triplets, Carbenes and Biradicals A Density Functional and Ab Initio Study”. In: *The Journal of Physical Chemistry A* 110.44 (2006), pp. 12267–12275.

[23] Sebastian Sinnecker et al. “Calculation of solvent shifts on electronic g-tensors with the conductor-like screening model (COSMO) and its self-consistent generalization to real solvents (direct COSMO-RS)”. In: *The Journal of Physical Chemistry A* 110.6 (2006), pp. 2235–2245.

[24] Frank Neese. “Calculation of the zero-field splitting tensor on the basis of hybrid density functional and Hartree-Fock theory”. In: *The Journal of chemical physics* 127.16 (2007).

[25] Lucas Lang et al. “Theory of Field-Dependent NMR Shifts in Paramagnetic Molecules”. In: *Journal of Chemical Theory and Computation* (2025).

[26] Letizia Fiorucci and Enrico Ravera. “Not Just Another Crystal Field Software”. In: *Journal of Computational Chemistry* 46.6 (2025), e70063.

[27] Enrico Ravera et al. “A quantum chemistry view on two archetypical paramagnetic pentacoordinate nickel (II) complexes offers a fresh look on their NMR spectra”. In: *Inorganic Chemistry* 60.3 (2021), pp. 2068–2075.

[28] Timothy N Abell et al. “Trispyrazolylborate Complexes: An Advanced Synthesis Experiment Using Paramagnetic NMR, Variable-Temperature NMR, and EPR Spectroscopies”. In: *Journal of Chemical Education* 94.12 (2017), pp. 1960–1964.

[29] MPM Marques et al. “NMR conformational study of the lanthanide (III) complexes of DOTA in aqueous solution”. In: *Journal of Alloys and Compounds* 225.1-2 (1995), pp. 303–307.